Analysis of the cavitation instabilities with time-resolved stereo and multiplane Particle Image Velocimetry

Kunpeng Long, Mingming Ge, Annie-Claude Bayeul-Lainé, Olivier Coutier-Delgosha

Analysis of the cavitation instabilities with time-resolved stereo and multiplane Particle Image Velocimetry

Kunpeng Long[1], Mingming Ge[2], Annie-Claude Bayeul-Lainé[1], *Olivier Coutier-Delgosha[1, 2]

[1]*Laboratoire de Mécanique des Fluides de Lille – Kampé de Fériet, Arts et Metiers ParisTech, Lille, France*

[2]*Virginia Tech, Kevin T. Crofton Dept of Aerospace & Ocean Eng., Blacksburg VA 24060, USA*

Abstract

The present paper is devoted to the analysis of the various instabilities of cavitation attached to a two-dimensional (2D) profile. Time resolved stereo Particle Image Velocimetry (PIV) was conducted in a small-scale 2D venturi type section, in different vertical planes in the streamwise direction, located at varying positions in the depth of the channel. These experiments enabled to obtain the time evolution of the three components of the velocity field in the cavitation area, and to derive the time-averaged gradients in the spanwise direction. Test cases at various Reynolds number were conducted, maintaining either the pressure or the cavitation number constant, to discuss the impact of these parameters on the flow. Then, the attention was focused on three distinct flow dynamics, namely sheet cavitation, where no large-scale instability can be detected, single cloud cavitation, where a large cloud of vapor is shed periodically at the rear of the cavity, and multi-cloud cavitation, where the process is more complex, as more than one clouds are shed downstream. The data reveal that the structure and the structure of the re-entrant jet, which is one of the primary mechanisms of cloud cavitation, is more complex than reported in the previous studies. Although the jet can be detected as an intermittent low speed reverse flow in the streamwise direction, it is actually made of successive vortices about the channel depth, which are convected downstream while expanding in the vertical direction, causing the cavity lift and thus contributing to its final split and the cloud shedding.

Keywords: Cavitation, instability, flow imaging, PIV, re-entrant jet

*Corresponding author, ocoutier@vt.edu

1. Introduction

The dynamics of cavitating flows has been studied extensively in the last decades, to elucidate its mechanisms and be able to mitigate its adverse effects in various engineering applications, such as naval propulsion, rocket engine pumps, or industrial hydraulic systems. Most of these effects are related to the unsteady character of cavitation: the sheet cavities attached to solid bodies or walls are often characterized by periodical or non-periodical large-scale oscillations. At the same time, the collapse of the cavitation bubbles generates some large amplitude pressure waves and micro-jets, so the condensation areas are submitted to complex unsteady mechanisms involving high-pressure fluctuations[1]. It results in phenomena like vibrations, noise, erosion of solid surfaces, an increase of hydrodynamic drag, and unsteady forces potentially prejudicial for the other components of the system. In order to reduce these effects, a good understanding of the small-scale mechanisms involved in these instabilities is required.

Therefore, cavitation has been extensively studied in cavitation tunnels in configurations of simple geometries such as two-dimensional (2D) foil sections or Venturi-type sections in order to improve the knowledge about the structure of the two-phase flow and the mechanisms that control its unsteady features[2-8]. It is a consensus that cavitating flows are systematically unsteady at some scale, as the area of condensation, i.e. where the vapor bubbles collapse, is intrinsically submitted to continuous phase changes, pressure waves, and velocity fluctuations. In addition, cavitation attached to solid bodies, which forms a so-called "cavity", is often characterized by instabilities at larger scales, such as an intermittent detachment of its downstream part, forming clouds of vapor bubbles, which are then convected downstream until they collapse under the action of higher pressure[9, 10].

Although several mechanisms have been mentioned to explain this large-scale instability, a re-entrant jet flowing intermittently from the cavity closure to its leading edge, in the vicinity of the wall, is believed to be one of the primary causes of the cloud shedding phenomenon (see figure 1). Forty years ago, Knapp, Daily, and Hammitt[11] provided a quite precise description of the flow at the rear end of a cavity, where the external flow re-attaches to the wall. This flow, which initially moves along the cavity, has locally the structure of a jet impinging obliquely upon the wall. The falling stream divides into two parts flowing parallel to the wall. One forms the so-called re-entrant jet, which moves upstream and contributes to the cavity break-off and cloud shedding[2, 3, 8, 12, 13]. The other one makes the flow re-attach to the wall[14].

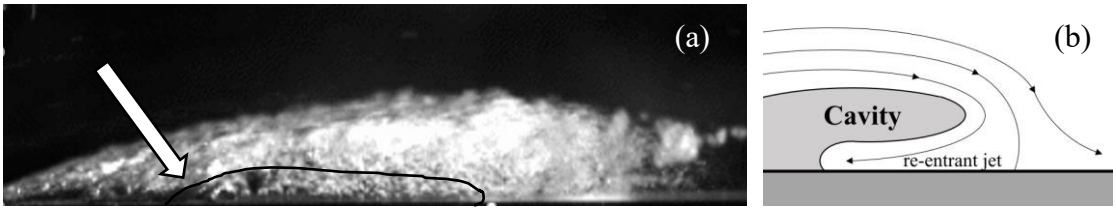

Figure 1. Re-entrant jet forming at the bottom of an attached cavity (flow from left to right) (a) snapshot of the jet, as it is flowing upstream, (b) Schematic representation of the jet inception in the closure region

To study the mechanisms of cloud cavitation, various intrusive sensors have been used in the eighties and nineties, such as electrical probes[9], optical probes[3,15], and endoscopic visulizations[16]. More recently, non-intrusive techniques such as Particle Image Velocimetry (PIV), X-ray imaging, and infrared imaging have been also applied. Optical PIV based on illuminations with short pulses of laser light sheets faces some major challenges, when it is conducted at the most usual scale of the test sections, i.e. between 5 and 20 cm of characteristic dimension. Indeed, the tracers illuminated by the light sheet at the middle of the test section are masked by all the bubbles in between the middle and the side, so they can be hardly detected by the cameras. In addition, the laser light sheet is significantly disturbed by the bubble light reflections. These issues obviously become worse as the void fraction increases. Using fluorescent particles combined with filters that record only the fluorescent signal emitted by the tracers but not the laser light enables to partially fix them, but the quality of the images of particles is still poor inside the cavity. Conversely, an extensive analysis of the turbulence in the wake of the cavity, where the void fraction is small, could be conducted by Gopalan & Katz[17], and the flow dynamics outside from the cavity and in the cavity closure were also investigated[18-19]. The experiments performed by Dular et al.[20-21] have shown that setting the light sheet at a small distance from the side wall (typically a few millimeters) could enable to visualize the fluorescent particles inside the cavitation area and thus access the entire flow dynamics. However, in that case the measurements are limited to the boundary layers of the side walls, and thus do not reflect the most interesting dynamics of the flow.

X-ray imaging is an interesting alternative to optical PIV, which enables to get rid of some of the limitations mentioned hereabove, since x-rays penetrate straight into the liquid/vapor mixture. Therefore, all issues related to the reflections on the bubbles are suppressed. Combining fast x-ray imaging with PIV has enabled to obtain some first measurements of velocity inside the high void fractions areas[21], for both the liquid phase and the vapor one. However, this technique suffers from

several limitations as well, such as the small field of view, imposed by the size of the beam cross section, which does not enable to capture the entire dynamics of the sheet cavities. Another drawback is the quite small number of pictures that can be recorded in a row, imposed by the constraints related to the scintillator integrity, and also the integration of the results in the beam direction, which means that both the far field and the boundary layers are included in the particle motion recorded on the pictures.

These various experimental studies, either based on optical or x-ray imaging, have confirmed the presence of the re-entrant jet in configurations of periodical cloud cavitation, and the correlation between its propagation upstream, up to the cavity leading edge, and the cloud detachment[20, 22, 23]. Some other works have revealed the importance of other mechanisms to explain the cavity break-off, such as a condensation shock that propagates from the cavity closure to its upstream end, as shown by Ganesh et al.[24]. Perturbations at the cavity top interface have been also discussed for a long time[25] and the evidence of the development of Kelvin-Helmholtz instabilities has been recently provided by Dular et al.[26]. Three types of driving mechanisms have been identified by Zhang et al.[27], using a combination of x-ray and laser-based illuminations: the re-entrant jet, the condensation shock mentioned previously, and a pressure wave generated by the collapse of the clouds of vapor.

Some other investigations have also shown the existence of more complex instability modes, where the frequency of the jet is not necessarily equal to the frequency of the cloud shedding[28]. More generally, it has been shown that the re-entrant jet is present at the bottom of the cavity even in the case no large-scale fluctuation is observed. Some authors have suggested that a sufficient momentum of the jet was required to reach the cavity upstream end, and thus trigger the break-off[23], but the exact mechanisms that lead to the different flow instabilities observed in the experiments (a rather stable cavity or regular cloud cavitation, or irregular cloud shedding with multiple small clouds) are still unclear.

In addition, these previous works have been performed using single point acquisition tools or 2D field velocity measurements. The three-dimensional character of the flow structures involved in the re-entrant jet motion and the cavity break-off has not been properly characterized, yet. Callenaere et al.[11] have observed the re-entrant jet and the cavity oscillations, using top and side views, but no quantitative measurements of the 3D effects in sheet/cloud cavitation are available, to the best of our knowledge. In the present paper, the objective is to remedy to this situation by performing time-resolved 2D3C PIV based on laser illumination, to characterize the three-dimensional structures

generated by cavitation and analyze their dynamics for different types of instability regimes.

Section 2 presents the experimental setup, the PIV acquisition settings, and the post-processing to obtain the three components of the velocity fields; section 3 is focused on the characterization of the different regimes that were identified, while section 4 discusses the 3D structures observed in these different cases, and their dynamics.

2. Experimental setup and image post-processing

2.1 Test Rig

Cavitation tests were conducted in the small-scale cavitation tunnel schematically represented in figure 2. Water circulation is obtained with a Salmson type Multi HE1602-SE-T/2-2G pump with variable rotation speed controlled by a micro-AC Variable Frequency Drive (VFD) model GS2-45P0 to set the flow rate. A tank partially filled with circulation water is used for water cooling at the pump delivery to maintain a constant temperature, using a secondary cooling loop. The volume flow rate is measured by a Bürkert type SE32 turbine flow meter (uncertainty 0.15 l/min after in situ calibrations), and the temperature is obtained with a type K thermocouple, directly in contact with the circulation water.

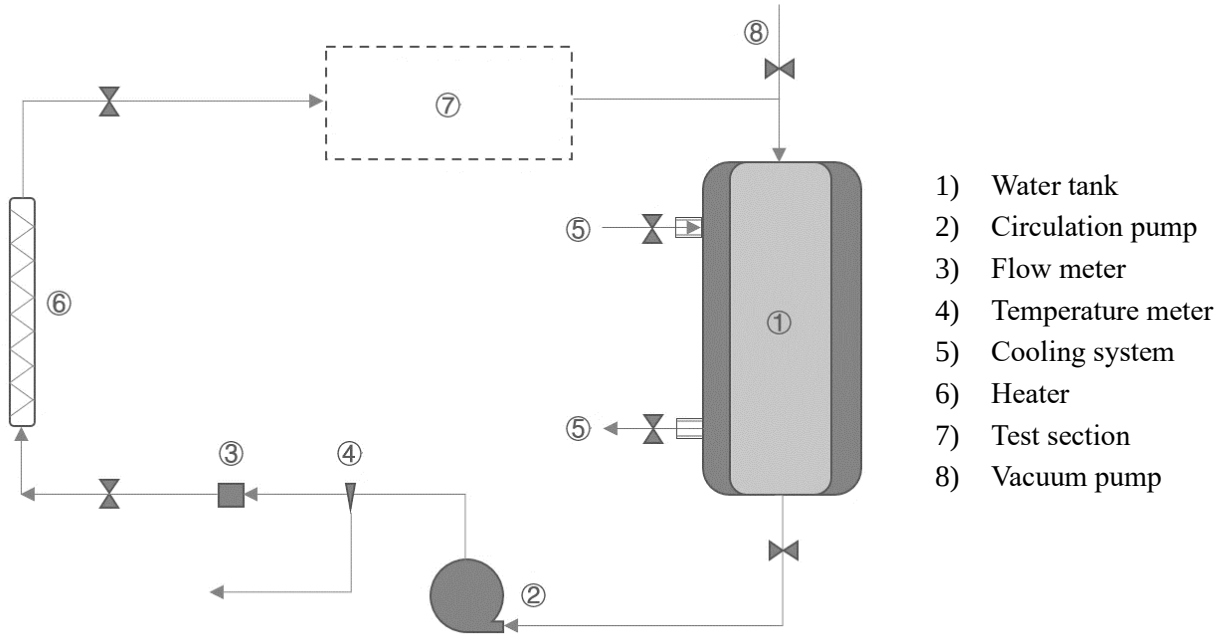

Figure 2. Cavitation tunnel

Upstream from the test section, a noise attenuation device is used to filter the periodical pressure fluctuations due to the passage of the pump blades. The reference pressure is measured 10 mm

upstream from the venturi test section with a Series 6M/S(C) OEM pressure transducer connected to a EV 94 EB digital indicator. The uncertainty on the measurements was of the order of 50 Pa. Another pressure meter measures the downstream pressure 10mm downstream from the test section. The partially filled tank is connected to a compressor and a vacuum pump, which enables to vary the pressure in this tank between 0.1 bar and 3.5 bar, thus adjusting the pressure in the test section.

2.2 Venturi-type Section

The main body of the test section is 3D printed, while the bottom, top, and side walls of the convergent / divergent nozzle are inserts made of transparent optical glass (figure 3). The venturi shape (bottom wall) is a simple wedge: the flow is accelerated in the convergent part of the venturi, which has a 18° angle. The maximum speed at the throat (width 5 mm, height 10 mm) is in the range from 10 to 20 m/s. Cavitation is initiated immediately downstream from the edge of the Venturi, which has an 8° divergence angle, and it collapses abruptly as the fluid moves outwards, since the pressure re-increases downstream.

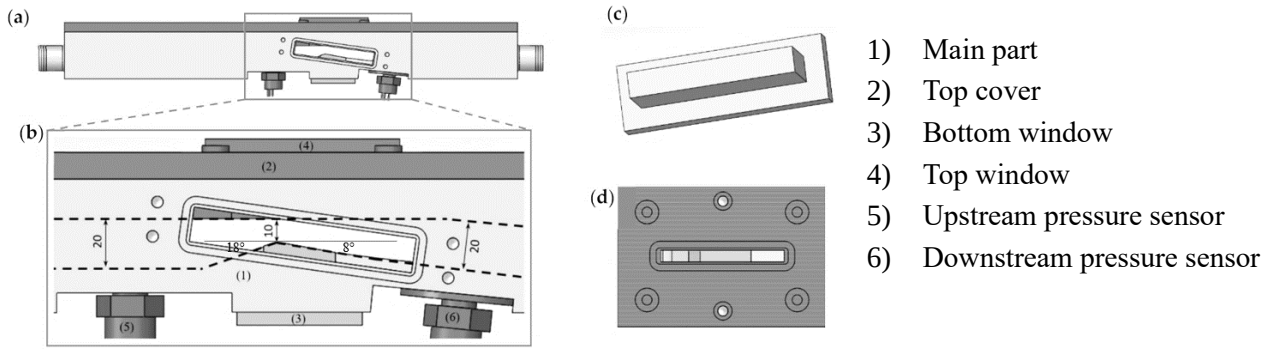

Figure 3. Venturi-type section: (a, b) side views, (c) side window, (d) top window

2.3 PIV measurements

The flow field is illuminated from the top with a vertical light sheet generated with a Nd:YAG 300 mJ/ pulse dual-head laser (figure 4). The light sheet is about 1 mm thick and is located at the middle of the test section. The flow is seeded with PMMA-RhB-Frak Fluorescent tracers with an average 10 µm diameter, which re-emit light at a wavelength 584 nm, significantly higher than the original 527 nm of the laser.

Two Photron FASTCAM SA1.1 and two Phantom VEO 710 high-speed cameras were used to capture images from the two sides of the test section, as shown in figure 4. The cameras on the front

side are equipped with a notch filter that eliminates the wavelengths around 527 nm, in order to capture only the light emitted by the particles, while the cameras in the back have density filters that attenuate the light reflected by the cavitation bubbles, to avoid over-illumination. So, images of particles are recorded at the front for velocimetry in the liquid phase, while images of cavitation are obtained at the back, for velocimetry in the gas phase. On each side, the two cameras are oriented with an angle around 25 to 30 degrees from the direction perpendicular to the windows, which was found to be the best compromise between the accuracy of the velocity 3rd component and the sharpness of the images.

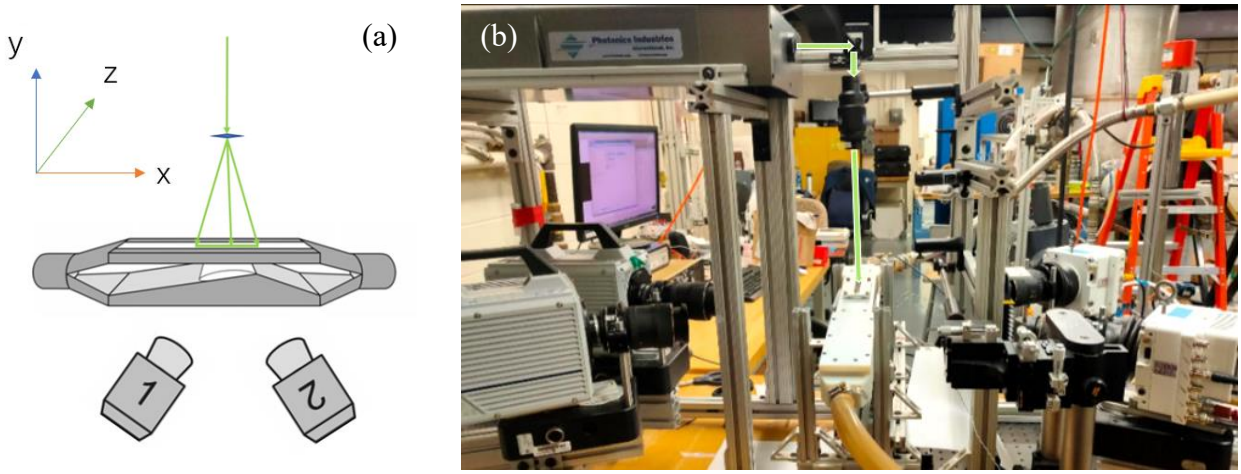

Figure 4. (a) Scheme of the venturi, (b) PIV setup

The laser generates two short pulses with a 7µs time interval, at a repetition rate of 2500 Hz. The four cameras and the light sheet were synchronized using a high-speed controller operated with the LaVision Davis 8.4 software, so 8-bit images were recorded at the same frequency with resolution of 1024×512 pixels (figure 5). The images of particles obtained with the notch filter still include the trace of the sheet cavity (see on the left), while the images of cavitation recorded with the density filter do not capture the tracers, due to the much lower intensity of the emitted fluorescence, compared with the light reflected by the bubbles.

The bright spot generated by each particle is typically 20 to 50 µm, i.e. 1 to 3 pixels on the images. Note that it's about 2 to 5 times the size of the particles only, as the spot is due to the fluorescence emitted by the particles, not the reflection of the incident light, so the halo generated by each particle is significantly smaller.

On the images of the vapor phase, the bubble interfaces cannot be clearly visualized: the smallest gas structures that can be seen are conglomerates of several bubbles. However, these vapor structures

generate some significant gradients of brightness, which will enable efficient post-processing to get the velocity fields, as explained hereafter in section 2.5.

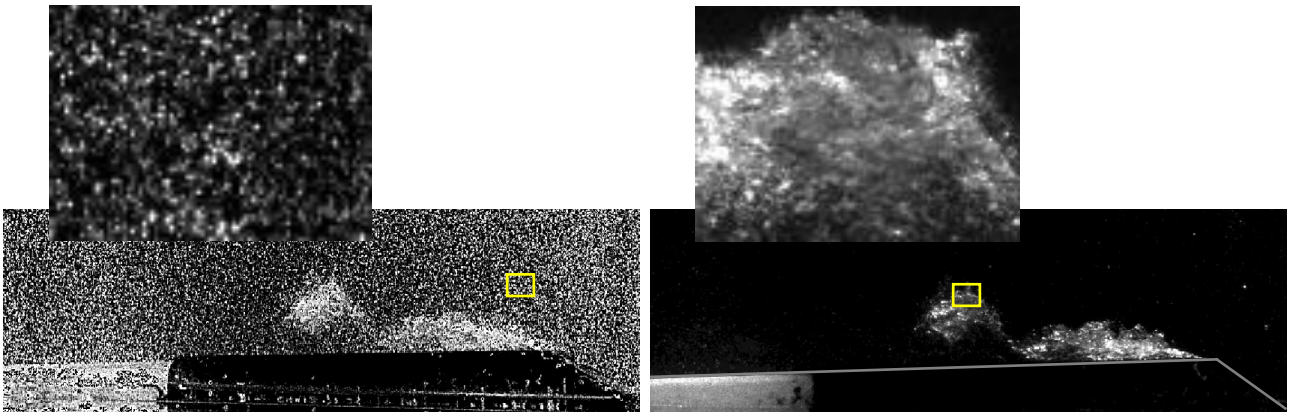

Figure 5. PIV raw images: water phase (left) and vapor phase (right)

In order to perform measurements in different planes in the z direction (see figure 4), the test section is mounted on a sliding frame controlled with a micrometric screw of precision 0.01 mm, to adjust precisely the laser light sheet position, from the front side to the back side (5 mm distance with 0.5 mm between two successive positions). This setup enables moving only the test section without changing anything in the PIV setup. Note that the test section was fixed rigidly to the frame, so that only the entire frame could slide, but no other motion was enabled, which was critical for the accuracy of the calibration.

A thorough calibration process was performed, once the laser light sheet, camera fields of view and image sharpness were adjusted: the test section was moved so that the light sheet was at the middle of the channel, then the top (see figure 3b) was open to the air, but still maintained full of water. A micro calibration plate from LaVision (200 µm distance between the dots, covering the 25×10 mm^2 surface of the field of view) was inserted into the test section and used to record the calibration data. The micrometric screw was used to move the test section to the front and the back, for the need of the stereo PIV calibration. Once the process was completed, the test section was closed for measurements.

2.4 Test cases

A first experimental campaign (not used in the present paper) has enabled to identify different types of cavitation regimes for various Reynolds numbers between 10^5 and 2×10^5, by varying the

flow rate from 30 up to 60 l/min, and for various cavitating numbers from 0.85 (large cloud cavitation) up to 1.4 (cavitation inception). The Reynolds number is $Re = h \times V_{th}/\nu$ where h = 10 mm is the channel height at the venturi throat, V_{th} is the average flow velocity at the throat, and ν is the liquid kinematic viscosity at the ambient temperature. The cavitation number is $\sigma = (P_{in} - P_v)/\frac{1}{2}\rho V_{th}^2$, with P_v the vapor pressure, P_{in} the pressure measured upstream from the test section, and ρ the liquid density.

Based on this preliminary investigation, two different sets of data are eventually used in this paper. In data set #1 (table 1), the pressure in the tank downstream from the test section is the atmospheric pressure, so the cavitation number is varied with the flow rate. For each flow condition, five positions of the laser light sheet were investigated every 0.5mm, from the center line of the test section to 0.5 mm from the front wall.

Conversely, in data set #2 (table 2), the pressure is varied with the flow rate, using a vacuum pump/compressor, to keep the cavitation number the same at various flow rates. Nine positions of the laser light sheet were investigated (every 0.5 mm on both sides of the center plane of the test section).

Note that the test rig does not have any control of the density of nuclei or the amount of dissolved air. This could induce some spurious effect of the water quality on cavitation, especially when the installation is operated at low pressure. To avoid that, all the tests in each of the tables below were performed in a period of a few days, without changing the water, and after having operated the test rig continuously for several hours. This process was found to considerably reduce the risks of altering the sheet cavity at constant cavitation numbers. In the present study, no noticeable change in the sheet cavity length and oscillation frequency could be detected for identical flow conditions tested at the beginning and the end of the measurements.

Test case	T (°C)	P_v (Pa)	ρ (kg/m^3)	V_{th} (m/s)	Q (l/min)	Area (mm^2)	σ	P_{in} (Pa)	P_{out} (Pa)
1	28	3850	995.9	13	39	50	1.40	121500	92600
2	28	3850	996.2	14	42	50	1.23	123800	92400
3	28	3850	996.2	15	45	50	1.10	127300	92100
4	28	3850	996.2	16	48	50	1.00	131800	91700
5	28	3850	996.2	17	51	50	0.92	137100	90700
6	28	3850	996.2	18	54	50	0.87	144800	89500
7	28	3850	996.2	19	57	50	0.84	155000	87700

Table 1. Investigation flow conditions - data set #1

Test case	T (°C)	Pv (Pa)	ρ (kg/m^3)	V_{th} (m/s)	Q (l/min)	Area (mm^2)	σ	P_{in} (Pa)	P_{out} (Pa)
8	28	3850	996.2	17	51	50	0.85	126300	65700
9	28	3850	996.2	18	54	50	0.85	141000	69100
10	28	3850	996.2	19	57	50	0.85	156700	91400
11	28	3850	996.2	15	45	50	0.9	104700	61900
12	28	3850	996.2	17	51	50	0.9	133400	83600
13	28	3850	996.2	19	57	50	0.9	165800	109500
14	28	3850	996.2	15	45	50	1	115900	80300
15	28	3850	996.2	17	51	50	1	148000	104700
16	28	3850	996.2	19	57	50	1	183700	132200

Table 2. Investigated cavitation conditions – data set #2

2.5 PIV post-processing

The images of particles are used to get the velocity fields in the liquid phase, while the images of the vapor bubbles are used for the determination of the vapor velocity fields. In both cases, the calculations are performed using the Davis 8.4 software from LaVision, and the embedded calibration process described in section 2.3.

For calculations in the liquid phase, a preliminary pre-processing of the images is applied to eliminate the trace of the cavitation. It consists of particle brightness standardization and background filter to remove the effects of spurious global brightness variations. An example of the final images is shown in figure 6. As can be seen, in the final images, only the particles are visible, and the signal to noise ratio has been significantly improved, compared with the original images of particles shown in Figure 5.

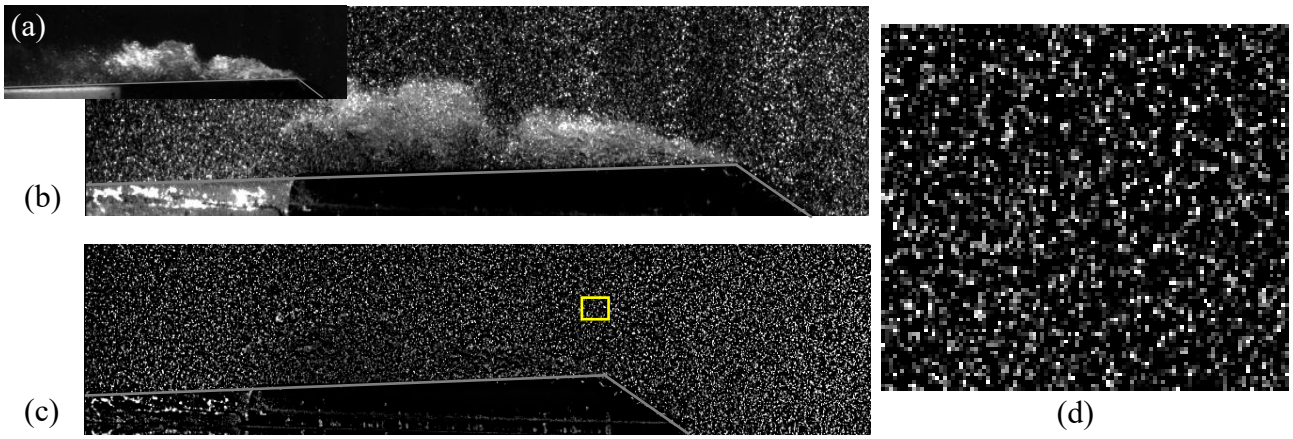

Figure 6. Pre-processing of the images of particles: (a) image of cavitation, (b) original image of particles, (c) final image of particles, (d) zoom

For calculations in the vapor phase, the image intercorrelation is not based on illuminated particles, but the gradients of brightness induced by the vapor bubbles. This specific application of PIV algorithms to velocimetry in the vapor phase has been tested and validated in previous works, using both optical imaging[29,30] and x-ray imaging[22,23]. An uncertainty of the order of 3% to 7% was generally obtained in these previous studies. It was found that such accuracy can be obtained only if local brightness intensity gradients are present in the bubbles, while post-processing based on images of interfaces only results in much lower accuracy. Note that this technique provides the speed of the bubbles, not the details of the internal flow inside them, although we will call these speeds "vapor velocities" hereafter in this paper.

For both the liquid and the vapor phases, five passes were performed, with interrogation windows of 64×64 pixels and 50% overlap for the first 2 passes, and 32×32 pixels windows and 75% overlap for the next 3 passes. Vectors with a correlation factor lower than 0.6 or a Q factor lower than 1.3 were discarded. The final results are smoothed by applying a 3×3 Gaussian kernel.

Figure 7 shows the typical uncertainty and correlation factor distributions that are obtained for the amplitude of the velocity, in both phases. As for the liquid velocity field, the correlation is about 0.8 in pure water, and it drops significantly in the mixture area, down to about 0.4 in the densest cavitation regions. Regarding the vapor phase, the correlation factor varies between 0.6 and 0.9 in the mixture, with most of the cavity in the range 0.7 – 0.8. Above the cavity, it drops to 0.3, as only a limited number of vapor bubbles are travelling in this region.

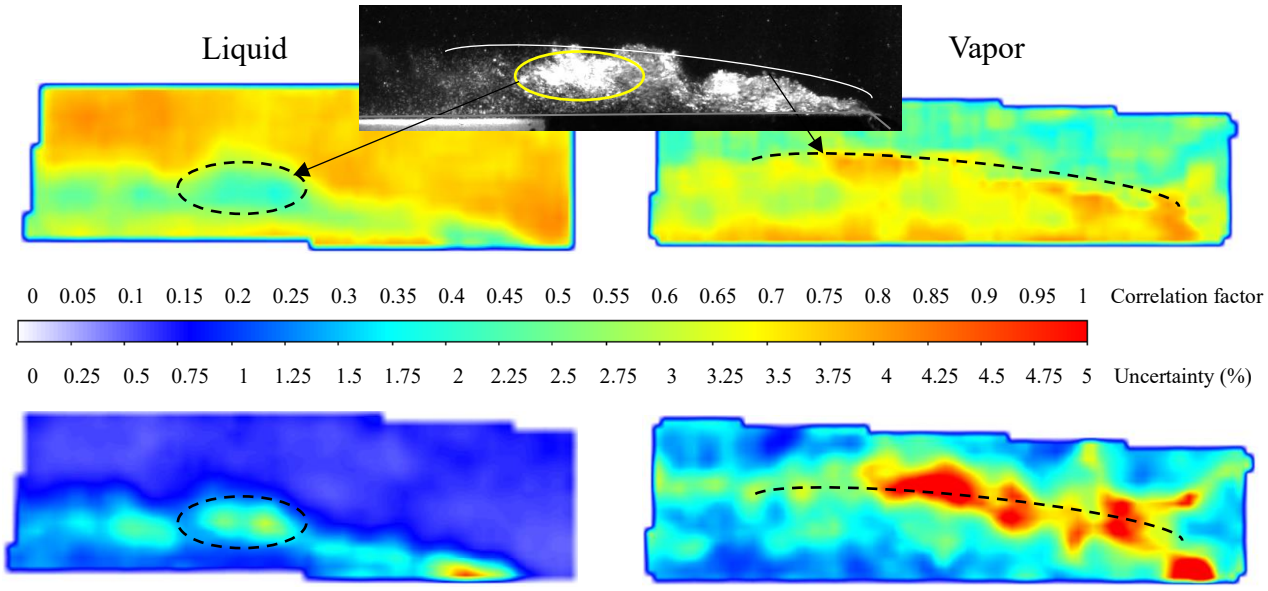

Figure 7. Typical correlation factor and uncertainties obtained in the liquid phase (left) and in the vapor phase (right)

Uncertainty is consistent with the variations of the correlation factor. Note that it is calculated by applying half of the calculated velocity field to the first frame of the pair, and -half to the second frame, and performing an intercorrelation of the two resulting images. The results are made non-dimensional using the local calculated velocities, which results in the uncertainties shown here. As can be seen, it is generally in the range of 0.5 to 2%, except in specific areas: the upstream end of the cavity for the liquid phase, due to the large void fraction that does not enable to detect as many particles as in the other areas, and the cavity interface for the vapor phase, as this is where the void fraction and thus the correlation factor abruptly drop.

It can be observed in Figure 8 that this uncertainty in the liquid phase is mainly driven by the z component (perpendicular to the light sheet), while the x and y components have uncertainties lower than 1% in most of the cavitation area, and even lower than 0.5% in the half part the closest to the wall. The exact same trend can be observed for the vapor phase as well (not shown here). Note that the conclusions drawn from figures 7 and 8 generally apply to all the velocity calculations (with some space modifications due to the time evolution of the cavity) and to all the test cases listed in section 2.4.

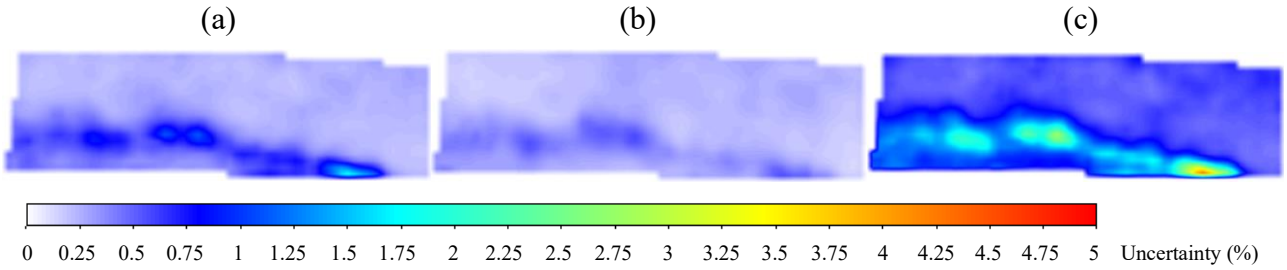

Figure 8. Uncertainty on the three components of the velocity in the liquid phase

(a) V_x, (b) V_y, (c) V_z

2,500 pairs of images (1 s of time) were recorded for each position of the laser light sheet. This number was found to be appropriate regarding the convergence of the time-averaged components of the velocity, as can be seen in figure 9. Obviously, the z-component is the one that requires the largest time to converge, especially in the re-entrant jet area where the flow is highly fluctuating.

The time-averaged values of velocities will be analyzed first in section 3 to characterize the general structure of the flow and the different dynamics of the two phases, then the instantaneous flow fields will be used in section 4 to discuss the different modes of instabilities. In addition, Proper Orthogonal Decomposition (POD) will be applied to help identifying the flow dynamics in section 4.

Typically, the flow based on the first 400 first modes will be examined. It enables taking into account 90% of the flow energy, while filtering out the most chaotic part of the flow fluctuations in order to isolate the periodical structures.

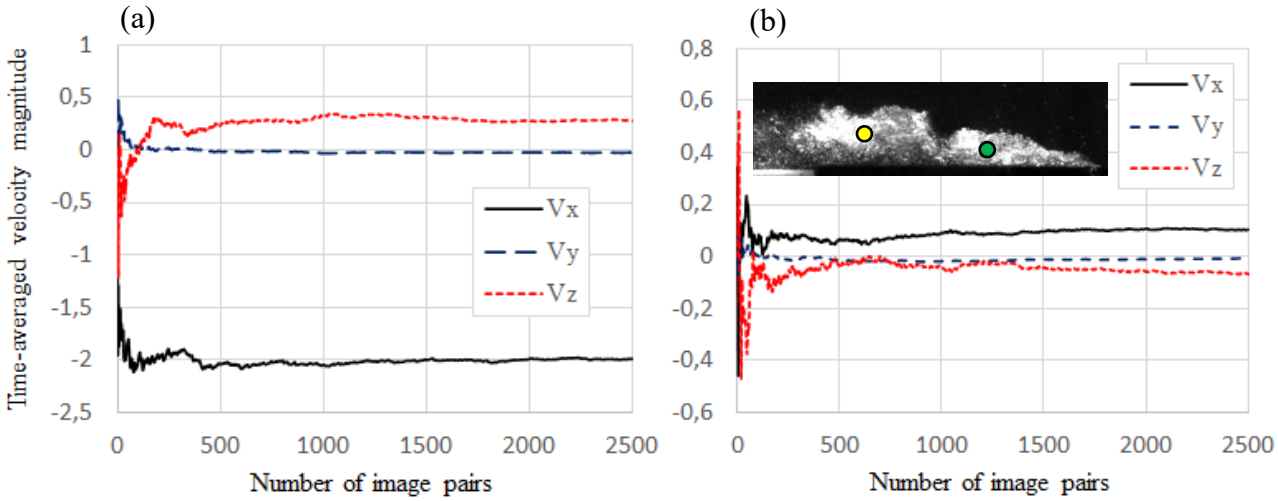

Figure 9. Convergence of the time-averaged velocity components according to the number of image pairs: (a) in the cloud of vapor (yellow dot), (b) in the re-entrant jet (green dot).

3. Flow structure and general dynamics

3.1 General flow structure

The incoming flow was characterized by measuring the time-averaged V_x velocity component and the turbulence intensity along a vertical profile located at the throat of the Venturi. Two flow rates (45 l/min and 57 l/min) are considered, to check the influence of this parameter on the velocity distribution. At 57 l/min, measurements were done in five different vertical planes, from the center of the test section to the front side, to check the flow homogeneity both vertically and horizontally.

Figure 10 shows that the flow is pretty homogeneous in both directions and both flow rates: the velocity is almost constant in the top half of the test section, while it slightly increases down to the bottom, by about 3% at 45 l/min and 7% at 57 l/min, due to the local flow acceleration. Horizontally, the velocity decrease from the center to the last position on the side is less than 5%, so it is concluded that the incoming flow is quite two-dimensional and uniform.

The turbulence intensity is mostly in the range 2 to 3.5%, except at the very bottom and in the top boundary layer, where it increases up to 5 to 6%. No major effect of the flow rate on these values is noticed, but the fluctuations are significantly enhanced close to the side wall, compared with the center of the test section, due to the influence of the boundary layer.

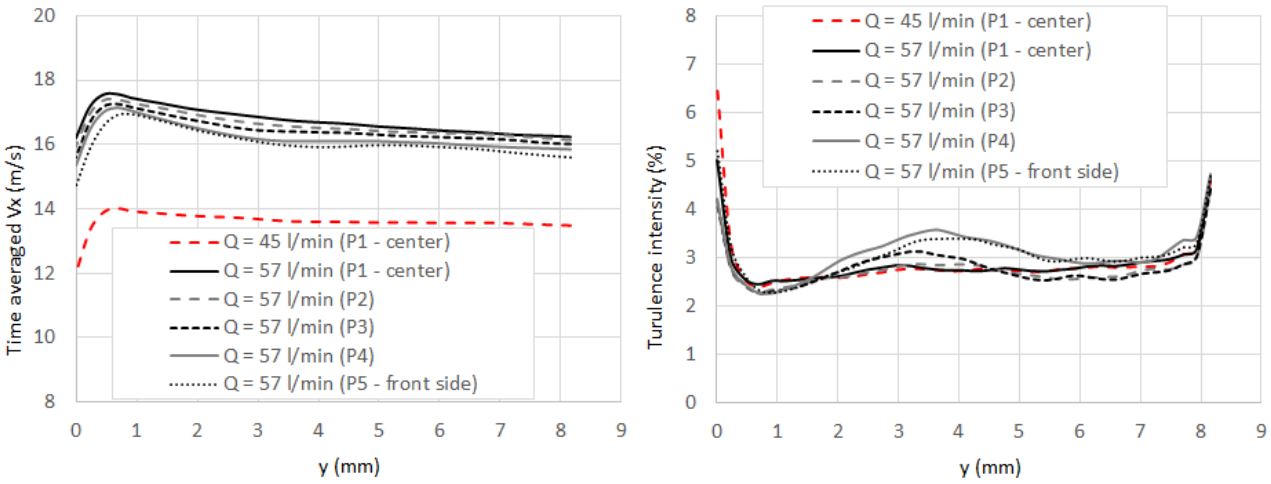

Figure 10. Inflow time-averaged velocity (x component) and turbulence intensity for flow rates of 45 l/min (center of the channel only) and 57 l/min (5 planes from the center of the channel to 0.5 mm to the side window, the distance between two successive planes is 0.5 mm).

3.2. Cavitating behavior

In data set #1, as various flow rates were applied at atmospheric pressure, the cavitation region increased progressively, and different behaviors were obtained (see figure 11). At the smallest flow rates (test cases 1 to 3), a small sheet cavity is observed with non-organized fluctuations and random cloud detachments in its rear part. As the flow rate is increased (test cases 4 and 5), the cavity significantly increases and the fluctuation becomes regular, with a large-scale periodical shedding. At the two largest flow rates (test cases 6 and 7), some irregularity affects these shedding, as multiple clouds are sometimes generated, which might merge or interact together. As a result, the oscillation frequency is not so clear anymore. These three distinct behaviors will be called sheet cavity, cloud cavitation, and multiple cloud cavitation hereafter, which is consistent with the names usually given in the literature.

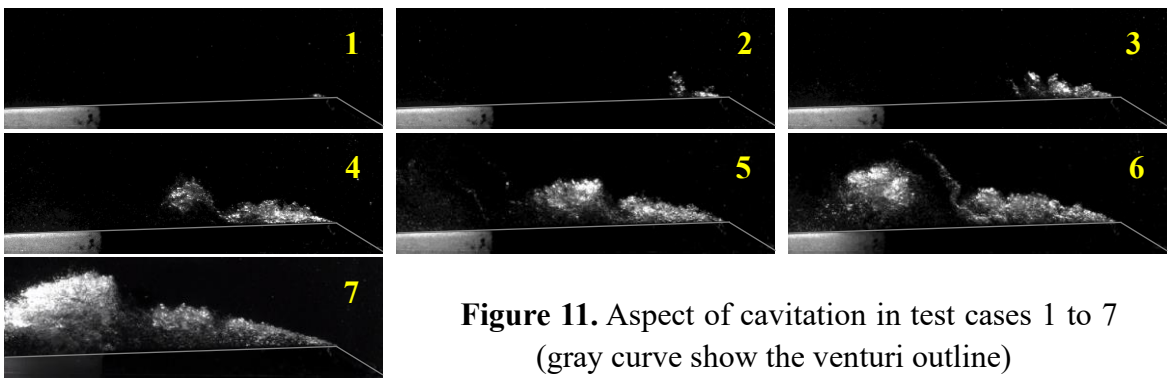

Figure 11. Aspect of cavitation in test cases 1 to 7 (gray curve show the venturi outline)

The flow field generated by the cavity is generally characterized by a large-scale recirculation, inducing a re-entrant jet in the vicinity of the bottom wall, as can be seen in figure 12. This is just a time-averaged behavior here, the flow unsteadiness will be discussed later. Also, note that only the liquid flow velocity is shown here, but the vapor flow is qualitatively very similar. A quantitative comparison between the dynamics of the two phases will be shown hereafter.

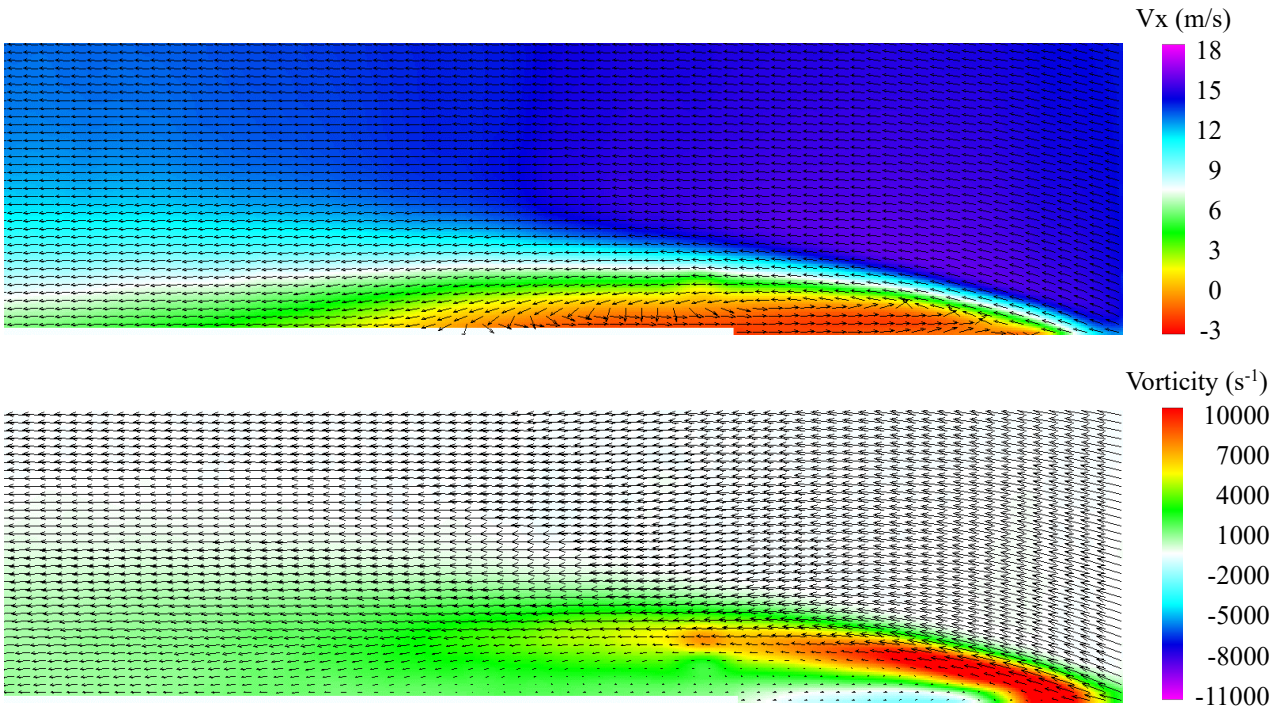

Figure 12. Example of the time averaged flow structure (test case #6, liquid phase). V_x velocity component with same length velocity vectors (left) and vorticity field with real vectors (right)

3.3. Effect of the flow non-dimensional numbers on cavitation

To discuss the flow dynamics at various conditions of operation, it is necessary to identify first which parameters impact cavitation. In that regard, the precise determination of the cavity length has always been a challenge in experiments focused on cloud cavitation, because of the fluctuating nature of the flow and the difficulty of finding a "limit" to the cavity. In addition, the flow illumination does significantly impact the conclusions: typically, in the case of laser light sheet illumination, the spanwise location of the light sheet is important, due to the three-dimensional shape of the sheet cavity. Figure 13a shows that different grey levels evolutions in the x direction are obtained in the 5 vertical planes located from the center to the front side of the test section: if this information had to be used to define a mean cavity length, the value would depend significantly on the selected position.

The same can be said about the cameras: the four cameras used in the setup record different levels of brightness, even if they were tuned to be similar. In conclusion, using this information to define the cavity length is very subjective.

In the present study the use of PIV has enabled to find a new appropriate way to define the mean cavity length. Indeed, figure 13b shows that the evolutions of both the maximum (in each cross-section) vorticity in the z direction, and the maximum positive speed of the re-entrant jet (note that everywhere the value is negative, there's no re-entrant jet) are very similar in the five vertical planes. Therefore, these quantities can be used, assuming that an objective threshold can be defined. Here, the location where the re-entrant jet vanishes downstream, i.e. the x value where there is no positive velocity in figure 13b, is selected as the end of the mean cavity.

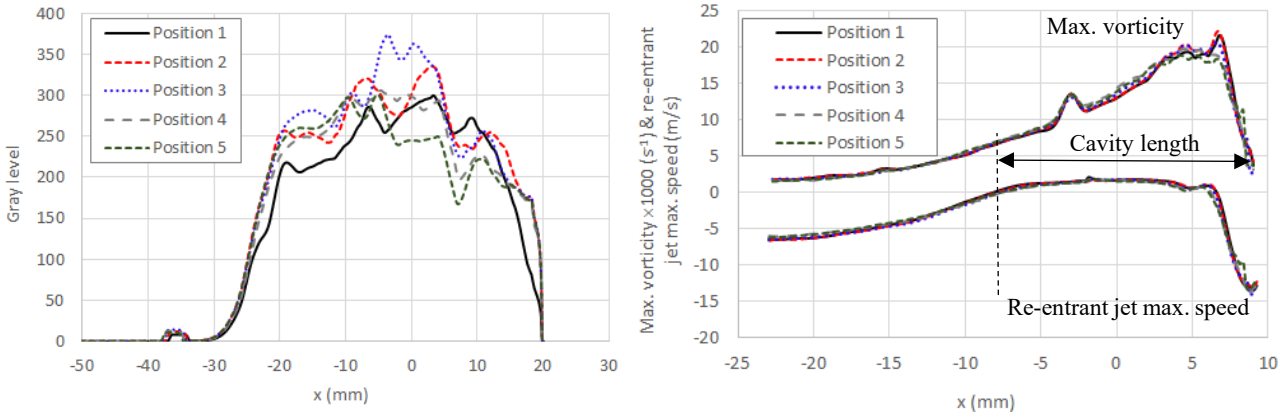

(a) (b)

Figure 13. (a) Max. gray level evolution in the flow direction, in the 5 vertical planes from center (position 1) to front side (position 5) of the test section; (b) Max vorticity and re-entrant jet max. speed evolutions, in the same 5 planes (test case #5).

The analysis of the effect of the flow parameters on the cavitation development has also generated a lot of contradictory conclusions in the last decades: the cavitation number is supposed to primarily determine it, however it depends significantly on the pressure used to calculate it, and it is also well known that the Reynolds number and the water quality, especially the amount of dissolved gas, also affect cavitation.

Typically, in the present study, it was found in the series of tests performed at constant σ number that increasing the Reynolds number systematically leads to a receding of the cavitation area (see figure 14). But the opposite effect was found by Coutier-Delgosha et al. 2005, for example.

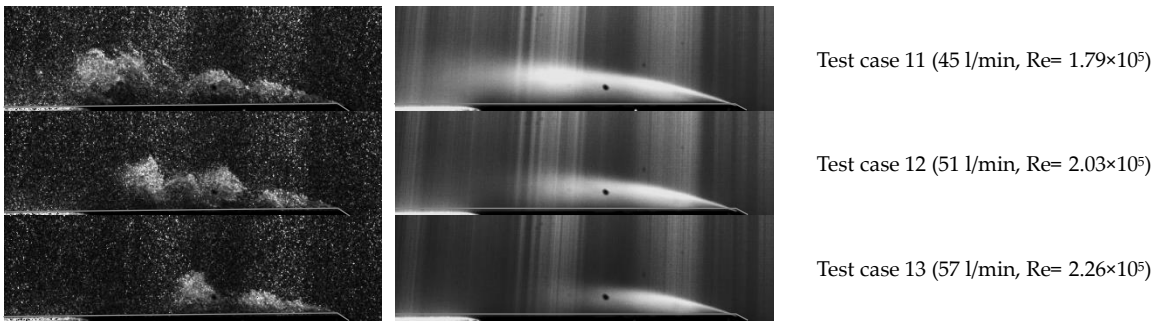

Figure 14. cavity length for σ = 0.9 and different flow rates – example of raw image (left) and time-averaged brightness (right)

To get a better idea of the differences between the 3 cavities shown in figure 14, the time-averaged flow field was investigated in more details. Although the general structure is very similar in the three cases, two significant modifications can be noticed (see figure 15): the amplitude of vorticity distribution increases with the flow rate, and the magnitude of the V_z component, i.e. the transverse recirculation, is also increasing. It suggests that the increase of the Reynolds number results in an amplification of the local pressure gradients that induce the vorticity and secondary flow in the z direction, also leading to the increase of the void fraction and the amplification of the periodical shedding intensity, as reported in previous studies by Coutier-Delgosha et al.[8]. The 3D effects observed here will be discussed in more detail in a second paper, so they are not detailed hereafter.

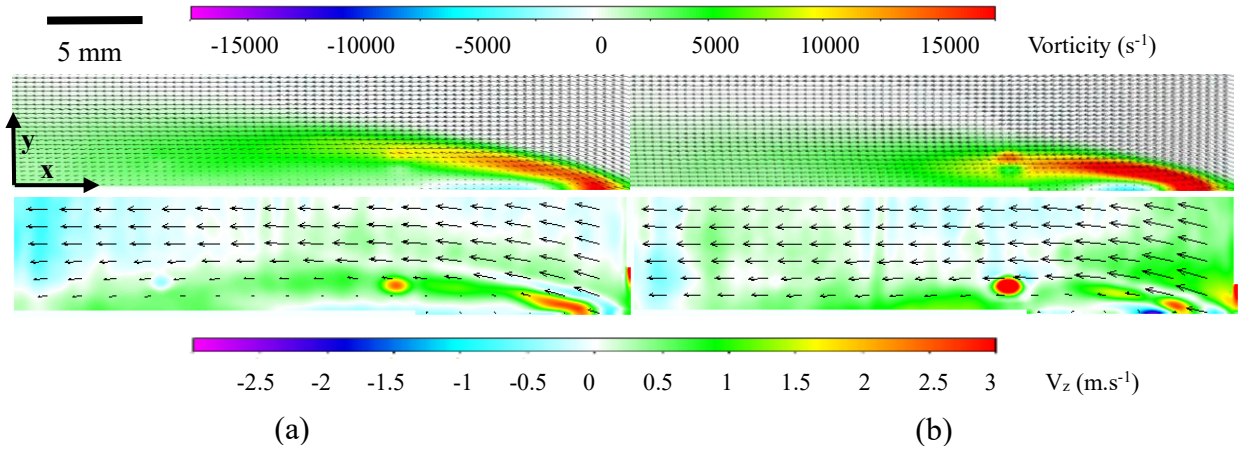

Figure 15. Comparison between cases (a) #11 (45 l/min) and (b) #13 (57 l/min) at σ = 0.9: the time-averaged vorticity field at the top, the time-averaged V_z velocity component at the bottom

It is believed by the authors that the exact position where the pressure is measured makes a significant difference in the impact of the flow rate on the cavity. Basically, any head loss induced by

the hydraulic loop in between the pressure tap and the cavitation area will vary with the flow rate and induce some bias in the calculation of the cavitation number, and thus in the way the cavity length will change according to the Reynolds number.

To avoid that bias in the present study, the average upstream and downstream pressure measurements (see figure 3 for their locations) are used instead of the upstream value. It is assumed that the resulting pressure is much closer to the one that would be measured downstream from the venturi throat, above the sheet cavity. The corrected cavitation number can be defined as $\sigma_{corrected} = \left((P_{up} + P_{down})/2 - P_v\right)/\frac{1}{2}\rho V_{th}^2$

As a result, it can be observed in figure 16 that all data of cavity lengths and re-entrant jet lengths collapse to a single curve, for all values of Reynolds and $\sigma_{corrected}$ (see figures 16b, 16c), while it was not the case with the initial σ calculation (see figure 16a).

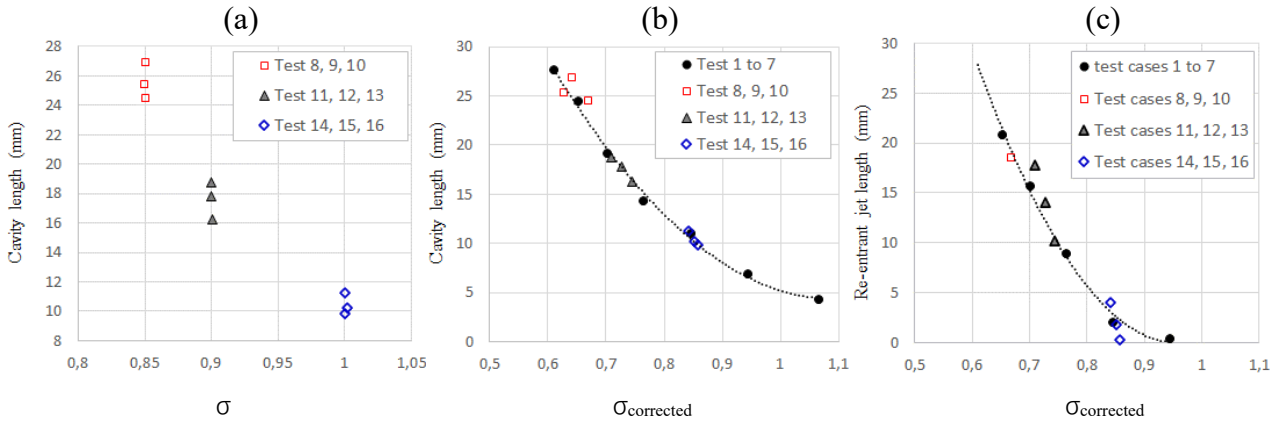

Figure 16. (a) Mean cavity length in all test cases, according to σ based on the upstream pressure, (b) same when $\sigma_{corrected}$ is calculated based on the average upstream / downstream pressure, (c) length of the re-entrant jet for $\sigma_{corrected}$ calculated based on the average pressure

3.4 Dynamics of the liquid and gas phases

It was usually assumed, until recently, that the liquid and gas phases have identical behaviors in cavitating flows. It was a reasonable hypothesis, as the size of most of the entrained bubbles are sufficiently small (a few microns to a few hundred of microns) to assume that they will be carried by the liquid flow without any slip.

However, it was found in the last ten years, using velocimetry based on x-ray imaging, that a significant slip between the two phases does exist in configurations of cloud cavitation[22,23]. It was suggested that the presence of big bubbles (typically up to 1 mm radius), the density of bubbles in such flows, which promotes bubble / bubble interactions and bubble cloud behaviors, and the

superposition of instabilities at different scales (from the large scale periodical shedding to the high-frequency turbulent fluctuations) could be responsible for this slip velocity.

No detailed information about this mechanism has been reported, yet, so the objective of this section is to use the present measurements to quantify in a better way how different the dynamics between the two phases are, and to discuss the reasons for these differences.

Test case #6 is primarily used hereafter, as it relates to a large sheet cavity, characterized with an intense and pretty regular cloud cavitation behavior, so it is a good candidate to identify the main features of the slip velocity field. Figure 17 shows a basic comparison between the liquid and velocity time averaged V_x and V_y components, respectively. Four profiles perpendicular to the bottom wall, located at x = 3 mm, 12 mm, 16 mm, and 24 mm downstream from the venturi throat, are used to draw the velocities. These 4 stations correspond typically to areas of (1) separation of the initial pure vapor zone into bubbles, (2) strong re-entrant jet progression, (3) detachment of the clouds of vapor, (4) convection of the clouds, according to the present observations and the conclusions previously reported by Zhang et al. (2020) in the same flow configuration, using high-speed x-ray imaging.

Note that the cavity shown in figure 17 is just a snapshot at a given time to show where the velocity profiles are located, but it does not reflect the entire area where vapor can be. The sheet cavity is highly fluctuating, so its shape changes over time, and bubbles and even bigger structures are travelling sometimes at higher y positions than what is shown here. It explains why a vapor velocity can be calculated up to 7.5 mm above the bottom wall, at stations 2, 3, 4.

Regarding the V_x velocity component, three main areas exhibit a significant slip velocity:

(i) the top half of the sheet cavity, where the vapor speed is lower than the liquid one. This is the main effect observed in the previous studies, which is related to the fact that the biggest vapor structures in this area are sometimes moving at a lower speed than the liquid. In other words, the biggest bubbles and the agglomerates of bubbles are not perfectly carried out by the main flow.

(ii) the very top of the profiles, where the vapor speed looks higher than the liquid one. It is believed that this is due to the time-averaging of the data, not to a physical mechanism. Indeed, at such height, vapor structures are only present from time to time, when the attached cavity gets temporarily thicker and/or generates a larger cloud detachment. In such a case, the liquid flow above the cavity experiences a reduction of the actual section of passage, and thus an acceleration, which impacts both the liquid and vapor phases. But on average, this effect only slightly impacts the liquid velocity, while it is the main part of the vapor velocity.

(iii) the vicinity of the wall, specifically at stations 2 and 3, where a larger vapor speed is also observed (either positive or negative). This might not be very clear in figure 17, but it will be confirmed hereafter in other vertical planes and for other flow rates. This third effect is related to the nature of the re-entrant jet. Indeed, it was reported in many previous studies, both from CFD and experiments, that the tip of the jet is an area of intense recondensation, while it flows upwards. It means that the front of the jet, where the speed is the highest, has a large density of vapor bubbles. Once these bubbles have collapsed, the velocity is lower, and that lower velocity is reflected only in the liquid velocity, not the vapor one. So, on average, it makes sense that the re-entrant jet area shows a larger vapor velocity.

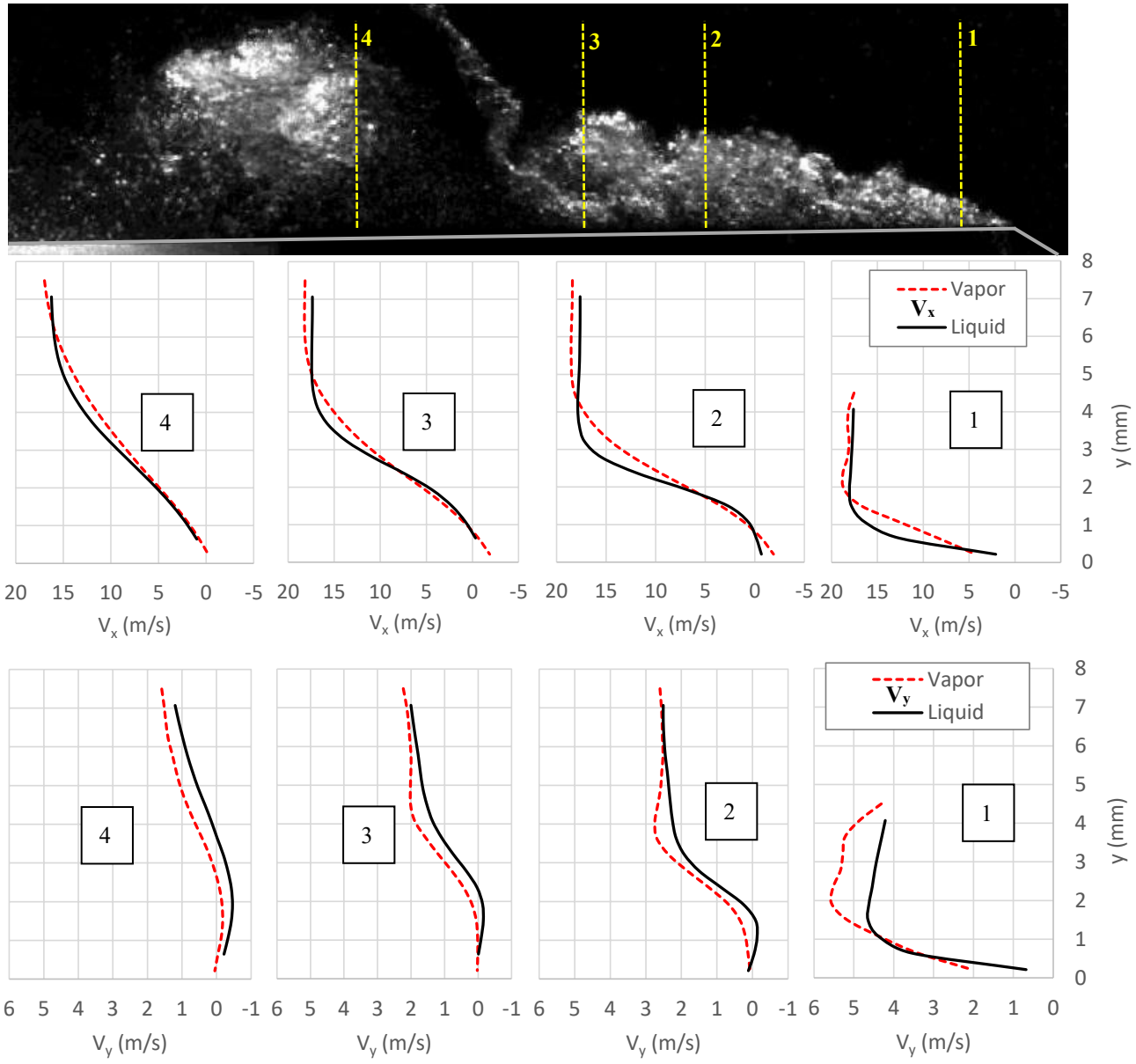

Figure 17. Time-averaged liquid and vapor Vx (top) and V_y (bottom) velocity components along the 4 profiles indicated at the top (Test case #6)

The V_y component generally shows a larger vapor speed as well, towards the positive y direction. It is related to the specific motion of the vapor structures which are moving up while transported by the main flow, and eventually form the large cloud of vapor, as can be seen by the global shape of the cavitation area. Conversely, the liquid flow is just following the basic expansion of the venturi section.

Figure 18 shows the non-dimensional slip velocity in the x direction, along the same vertical profiles, in four different vertical planes located from the center of the channel (P1 in black) to 5 mm off the front side (P4), again for test case #6. Generally, the observations reported here above in the middle plane also apply to the 3 other planes. The additional information provided here is that the slip velocity obtained close to the wall is more intense close to the side wall, compared with the center of the channel, at stations 2, 3, 4. It suggests that the side boundary layers do not slow down the bubbles as much as the liquid. In other words, the three-dimensional cavitation structures, as they are carried out by the main flow, are not completely responding to the local liquid speed variations: instead, their dynamics is impacted by the global motion of the vapor, such as the convection of the cloud of vapor.

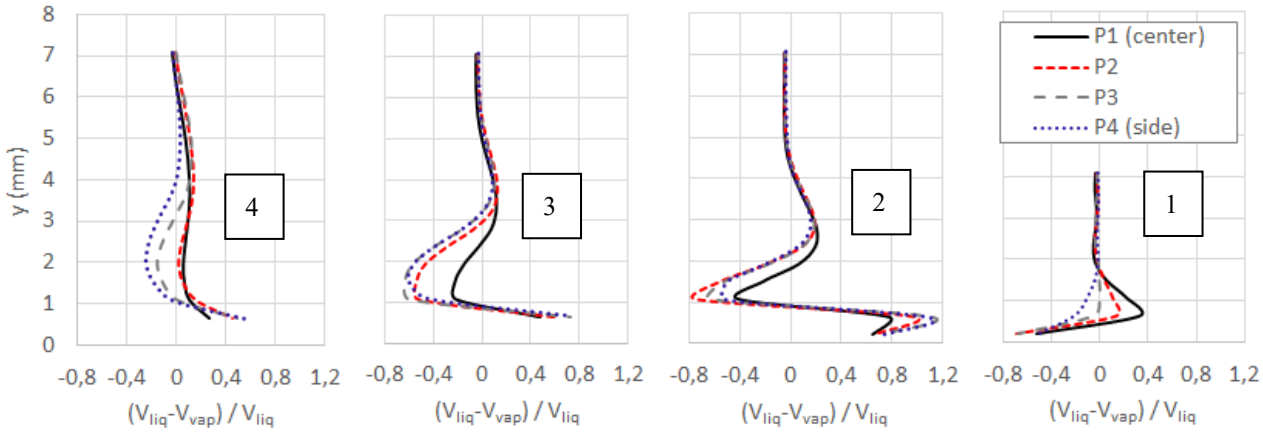

Figure 18. Time-averaged non-dimensionalized liquid and vapor Vx velocity component along the 4 profiles, in four different vertical planes located from the channel center (P1) to the front side (P4), 5 mm from each other (Test case #6)

The non-dimensional slip velocity variations obtained for V_x with test case #6 are very similar for all the flow rates investigated in this study. Figure 19 shows the data for test cases 1 to 6. When looking at this figure, we should keep in mind that the cavity size is not the same in these different test cases (see figure 11). At the lowest flow rates, only a small density of bubbles are convected downstream and generate the vapor velocity on these graphs, so it makes sense that the slip velocity

is very small along profiles 3 and 4, and progressively increases with the flow rate. More upstream, the same trend observed before repeats for all flow rates (positive slip velocity in the top half of the cavity and negative slip velocity close to the bottom wall), but it amplifies with the flow rate (although the values here are non-dimensional). It means that bigger cavities tend to enhance the specific dynamics of the vapor phase. This is also consistent with the explanation proposed for the slip velocity at the wall, since this effect should be stronger when the flow instability, and thus the re-entrant jet, is strong and regular, i.e. in typical cloud cavitation at flow rates 48 l/min and above.

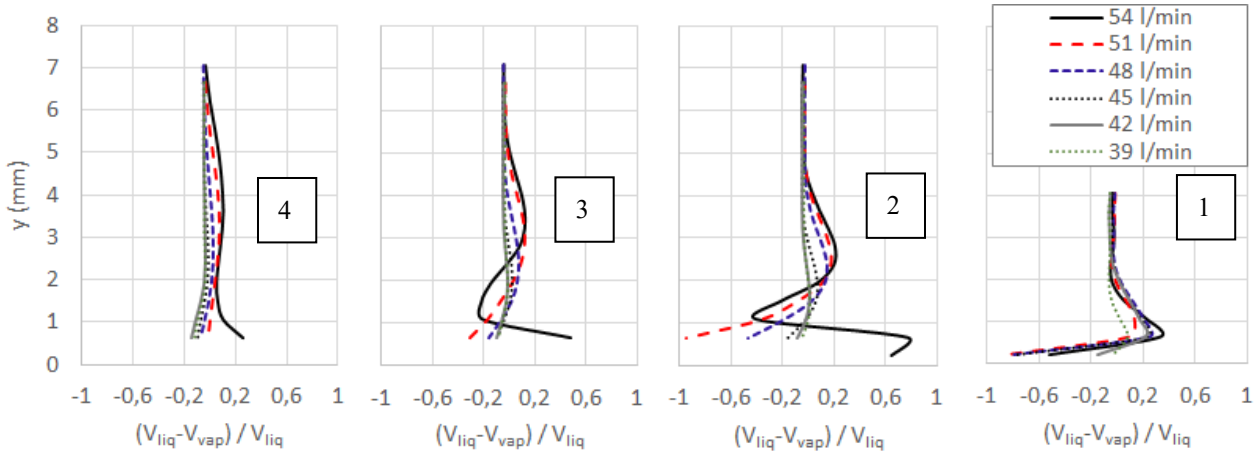

Figure 19. Time-averaged non-dimensionalized liquid and vapor V_x velocity component along the 4 profiles, in the vertical plane located at the center of the channel, for 6 different flow rates (test cases 1 to 6)

4. Investigation of the unsteady mechanisms

Generally, cavitation obtained in the present experiments can be divided into three different regimes: (i) typical cloud cavitation, where the cavity breaks off periodically and a single cloud of vapor is shed downstream, (ii) multi-clouds cavitation, where this instability generates more than one cloud, and (iii) sheet cavitation where the rear end of the cavity is affected by random fluctuations without shedding or just small non-periodical shedding. The present section is focused on these three regimes, using the PIV results in the liquid phase to discuss the mechanisms involved in each of them.

4.1 Single cloud cavitation

In the typical single cloud cavitation cases, the periodical unstable behavior of the cavity can be divided into four main stages, as shown in figures 20 to 23, which display the shape of the cavity, the

velocity fields (both in x and y directions) and the vorticity field at four different stages of a periodical cycle.

The first stage is the growing of the sheet cavity (figure 20). At this time, the previous cloud of vapor has detached from the main cavity and is convected downstream, while the remaining part of the sheet cavity is re-growing (see figure 20a). As shown in figure 20b, which displays the velocity field in the X direction inside the yellow dashed box indicated in figure 20a, a re-entrant jet (flowing from the left to the right with a positive velocity, see the red arrow) is clearly visible inside in the bottom half of the cavity, close to the wall. Note that the velocity vectors have all identical lengths, while the colors provide the magnitudes. Velocities up to 3 m/s are obtained in this area, while the main flow outside the cavitation area has a speed close to -20 m/s, and the rest of the cavity (in between the re-entrant jet and the pure liquid flow) is characterized by a sharp transition from -20 m/s up to a positive velocity.

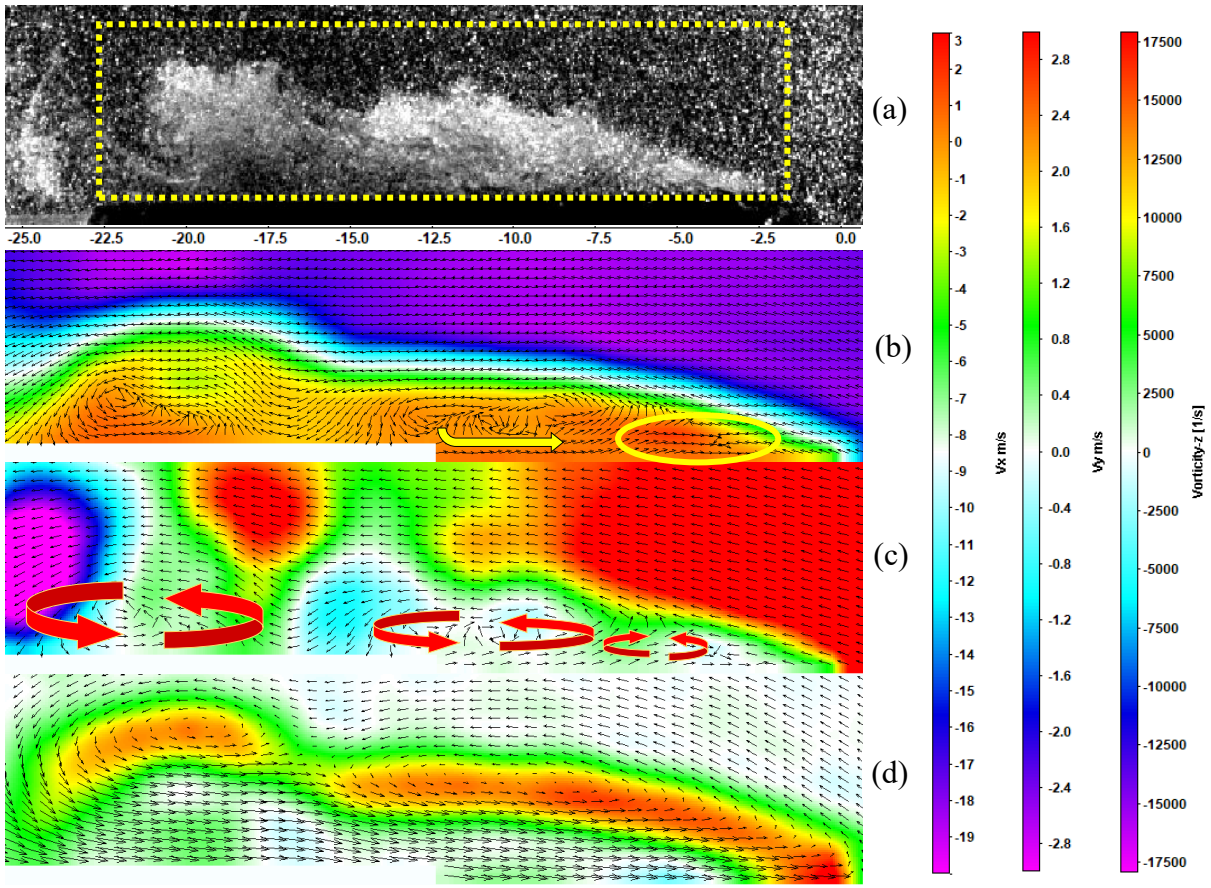

Figure 20. Stage 1 (cavity growing, T_0) in single cloud cavitation (test case #5). (a) Image of the cavity, (b, c) velocity field in the x and y directions, (d) vorticity fields. The velocity vectors are shown in pictures b, c, d with equal sizes, just to show the flow structure. In figure (d), it shows the relative velocity, so the time averaged velocity has been subtracted.

The re-entrant jet brings energy from the downstream area back to the upstream end of the cavity. It has been shown in previous studies[23,27] that the tip of the jet (see the red circle) is characterized by a significant recondensation of the flow, meaning that the vapor bubbles collapse, so the front of the jet is mostly liquid. It suggests that the tip of the jet is an area of higher pressure that triggers this recondensation (also called bubble shock wave by Ceccio et al.[5,6]). Most of the previous experimental data have identified the re-entrant jet as a time-averaged negative velocity along the main flow direction, just as we observe in figure 20b (see Stutz et al.[15]). However, it can be seen from the velocity field in the Y direction (figure 20c) that the re-entrant jet has a more complex structure. It is composed of a series of small vortices or small circulations (as shown in figure 20c and also on the vorticity field in figure 20d) about the Z direction, which are moving downstream along with the main cavity cloud vortex at speed from -6m/s (at the front end) to -19m/s (at the middle section), while expanding in the Y direction. Note that the velocity vectors have also an identical length, like in figure 20a, but fewer vectors are represented for the sake of clarity.

The second stage of the cycle is the up lift of the sheet cavity. As shown in figure 21a, a bulge of cavitation bubbles is formed in the second half of the cavity and starts to detach from the main cavity. At the same time, the re-entrant jet velocity decreases significantly (see figure 21b), becoming almost zero at the tip, which means that it nearly stops. This is due to the generation of a new intense vortex at the leading edge of the sheet cavity (see the blue circle in figure 21d), which blocks the progression of the jet. The series of vortices mentioned in step 1 are still moving downstream (see the red circle superimposed with the vorticity field in figure 21d), while the one at the most upstream position is pushed up, which initiates the break-off of the cavity. It can be assumed that the high pressure already mentioned at the tip of the re-entrant jet, combined with the additional increase due to the stopping of the jet, is responsible for this lift, which results in the formation of a local bulge in the cavity, and eventually its break-off.

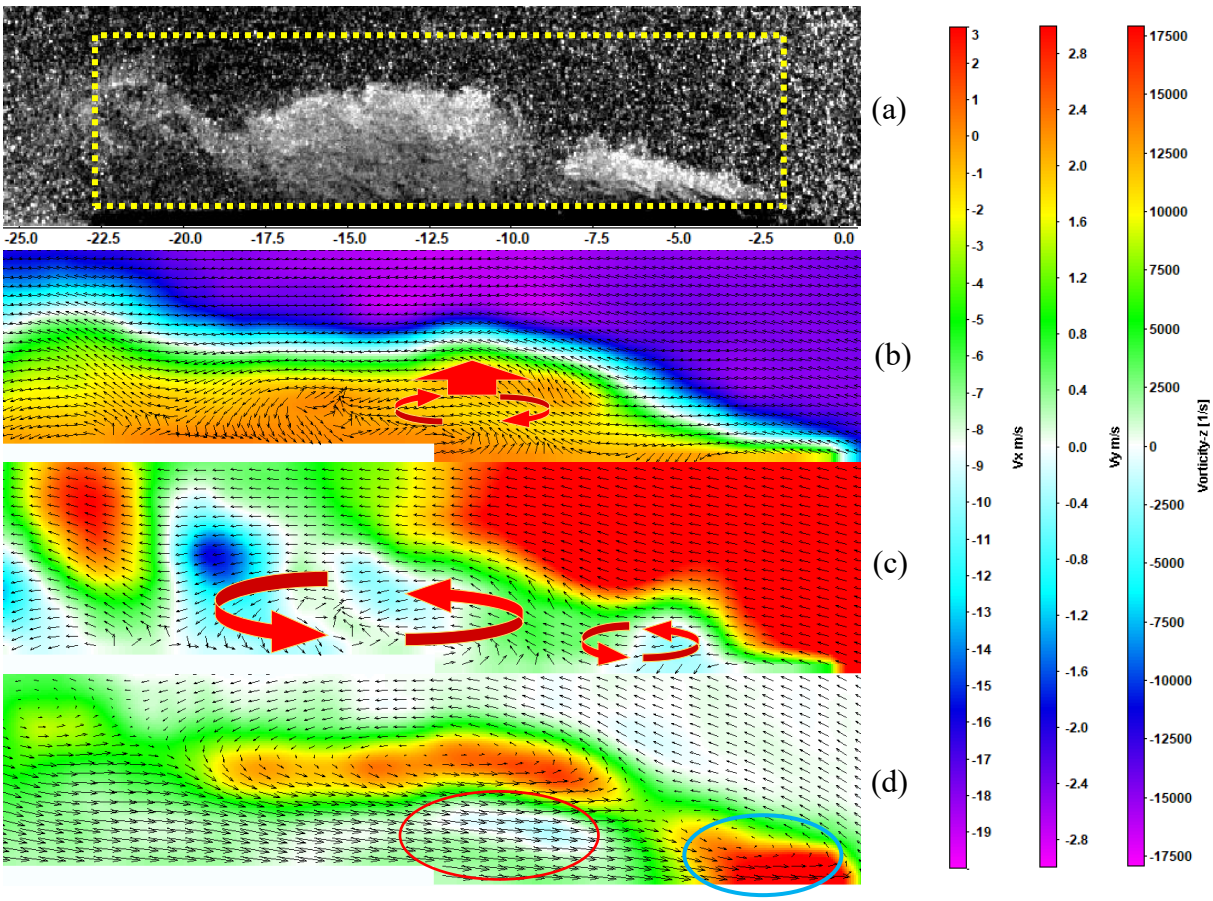

Figure 21. Stage 2 (cavity up lift, $T_0 + 0.4$ ms) in single cloud cavitation (test case #5). (a) image of the cavity, (b, c) velocity field in the x and y directions, (d) vorticity fields. The velocity vectors are shown in pictures b, c, d with equal sizes, just to show the flow structure. In figure (d), it shows the relative velocity, so the time averaged velocity has been subtracted.

The 3rd stage is the cavity break-off. As shown in figure 22a, the bulge continues to detach from the main cavity. Its front end is more and more lifted, while its back (downstream) starts to move to the bottom wall direction, resulting in a counterclockwise rotation. This rotation is due to the joint actions of a stronger re-entrant jet under the cavitation cloud (see the white circle in figure 22b) and the main flow above the cavity (see the yellow circle), which pushes the top of the cloud downwards.

As a result of this rotation, the bulge begins to roll up inwards, gradually forming a cloud-like structure, which is thus called a vapor cloud. At the same time, because of the blockage generated by this cloud, the flow above the cavity decelerates (see the left area inside the yellow circle) and deviates up and down, thus cutting the cavity interface and promoting the complete detachment of the cloud from the main cavity (as shown in the vorticity field in figure 22d). This “cut in” process can be used as a clear marker to distinguish a full cycle from a simpler cavity oscillation without any major cloud

generation. Moreover, this stage also shows how the re-entrant jet vortex system is formed and interacts with the main flow region.

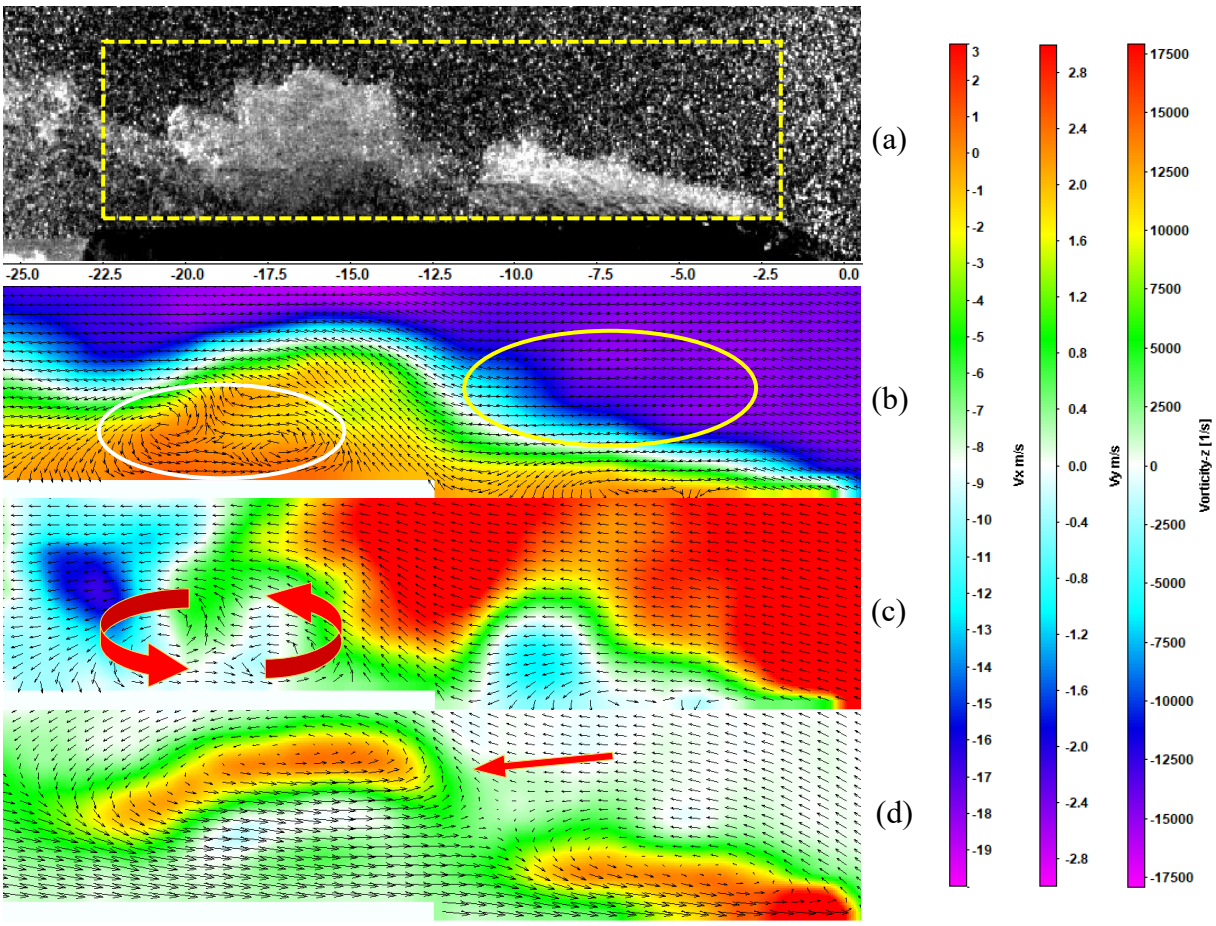

Figure 22. Stage 3 (cavity break off, T_0 + 0.8 ms) in single cloud cavitation (test case #5). (a) Image of the cavity, (b, c) velocity field in the x and y directions, (d) vorticity fields. The velocity vectors are shown in pictures b, c, d with equal sizes, just to show the flow structure. In figure (d), it shows the relative velocity, so the time averaged velocity has been subtracted.

The 4th stage consists of the convection of the detached cavity cloud. As shown in figure 23a, the cloud has already completely separated from the main cavity, and a new cycle is about to start. The velocity field in the x-direction (see figure 23b) shows that the re-entrant jet below the cavity cloud is almost completely suppressed by the vortex system, with only a tiny backflow far downstream (as shown by the yellow circle), while a new strong re-entrant jet is created at the back of the attached cavity (as shown by the blue circle). This implies that the re-entrant jet has the same periodic pattern as the cavity cloud shedding, in this flow configuration. The velocity in the y direction (see figure 23c) and the vorticity field (see figure 23d) show that the vortices in the re-entrant region below the

cloud of vapor are generating a shear flow between the cloud and the main liquid flow, which might contribute to the slip velocity observed in the previous section.

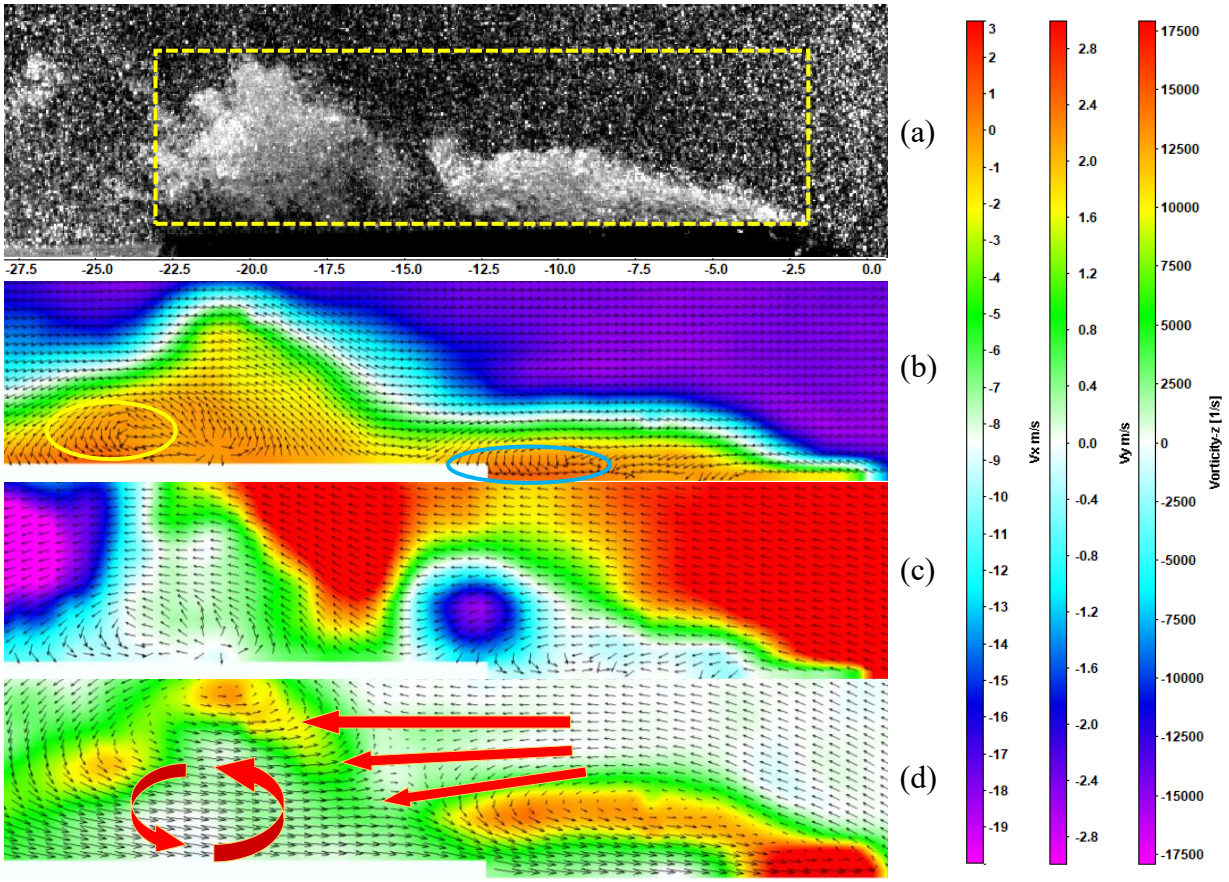

Figure 23. Stage 4 (cloud convection, T_0 + 1.2 ms) in single cloud cavitation at flow rate (test case #5). (a) Image of the cavity, (b, c) velocity field in the x and y directions, (d) vorticity fields. The velocity vectors are shown in pictures b, c, d with equal sizes, just to show the flow structure. In figure (d), it shows the relative velocity, so the time averaged velocity has been subtracted

4.2 Multi-clouds cavitation

In cases of large sheet cavities, several clouds are often generated and shed simultaneously, which is called here a multi-clouds configuration. In such cycles, the four stages described in the previous section still exist, but they are more complex and difficult to identify. Figure 24 shows a sequence of some raw images (in the middle), vorticity fields (left), and velocity fields in the x direction (right) to illustrate first the growing of the attached cavity.

At time T_0, it can be seen in the raw image that the previous cloud of vapor detached from the main cavity has been convected downstream and are collapsing, while the remaining part of the sheet cavity is re-growing. Frame 2 (T_0 + 0.4 ms) shows the growth of the new sheet cavity, but unlike the

typical single cloud cavitation, the sheet cavity does not create a distinct bulge: the whole sheet cavity is compact and thinner, attached to the bottom wall without any significant lifting effect. As the sheet cavity continues to grow (T_0 + 0.8 ms), a small bulge is created at the rear of the cavitation area (red circled area) and tends to detach from the main cavity area (see the yellow arrow). However, in the next frames 4 and 5, it is found that the detachment did not occur; instead, the bulge and the main cavity stretched, forming a long wavy single cavity. From T_0 to T_0 + 1.6 ms, the velocity field in the x-direction (on the right) shows a strong re-entrant jet close to the bottom wall, with a maximum velocity of about 3m/s. In contrast to the single cloud cavitation (figure 20b), this re-entrant jet is much thinner and has a higher speed, which is quite constant from the rear end of the sheet cavity to its leading edge. So, the jet does not slow down, which is likely related to the fact that its cross-section does not significantly increase, since the large bulge was not formed, in contrary to the single cloud case. Therefore, the cavity does not encroach too much into the main flow region, which allows cavitation to continue to grow throughout the entire process.

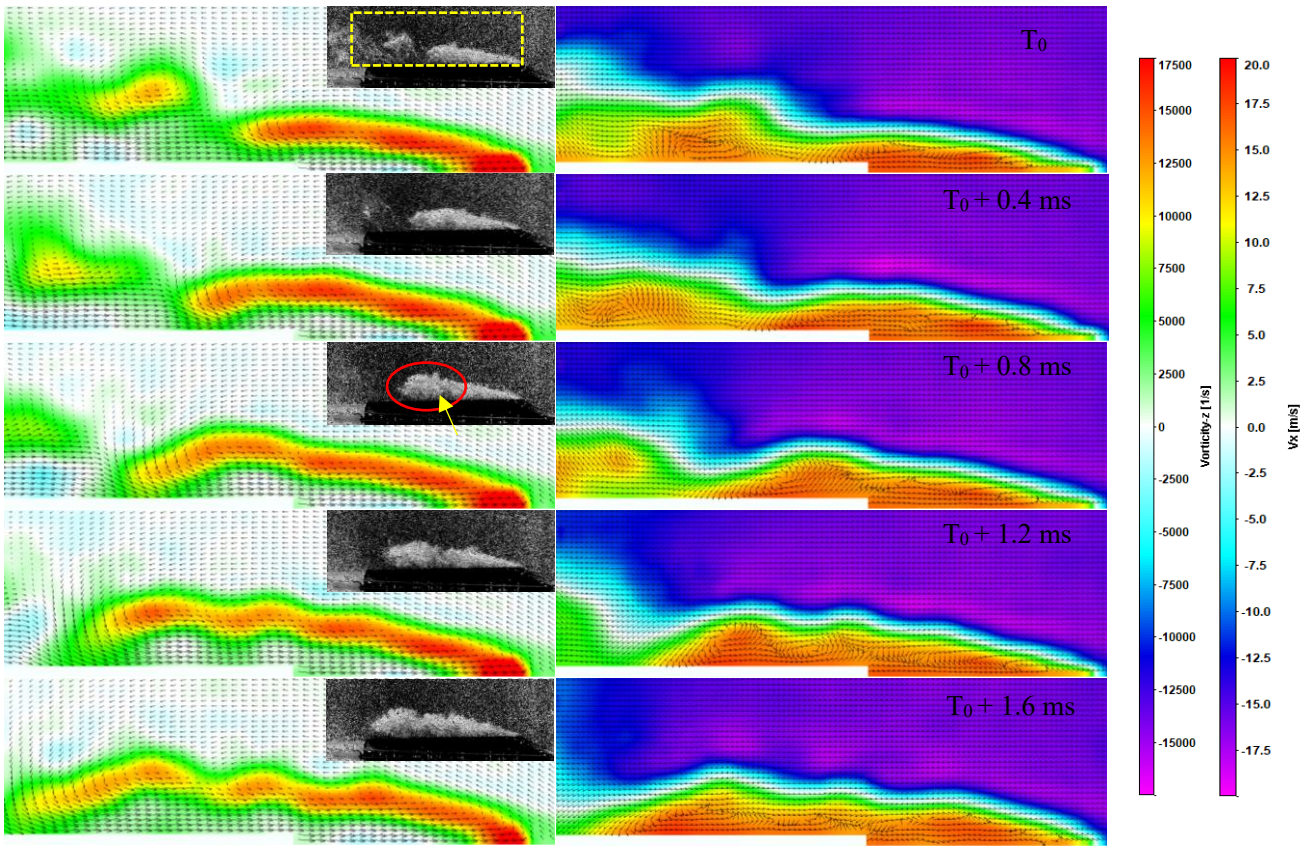

Figure 24. Growing of the attached cavity in the multi-cloud cavitation cycle at flow rate 54 l/min (test case #6) - Vorticity field (left), image of particles (middle), x-component of velocity (right) every 0.4 ms (T_0 is the start of the cycle, one period of the entire cycle is typically 5 ms)

In the next stage of the cycle (shown in figure 25 at T_0 + 2 ms), the situation starts to change, and a bulge can be observed in the middle of the wavy sheet cavitation (see the white circle in figure 25a). The velocity field in the x direction shows that at this point, the intensity of the re-entrant jet has severely decreased, and it has almost dropped to zero in the middle of the cavity (shown by the red circle). Due to this reduction of velocity, the local pressure rises, so a zone of relatively high pressure is formed in the middle of the cavity, like during the up-lift phase in single cloud cavitation (see figure 21b). This zone of high pressure creates a lifting effect (visible on the velocity field in the y direction in figure 25c, as shown with the blue circles) and therefore the bulge is created. Also, the vorticity field (figure 25d) shows in the bottom part of the cavitation region, a series of vortices that generate the wavy shape of the sheet cavity. This stage can be considered as the up-lift stage in the case of multi-clouds cavitation. However, unlike single cloud cavitation, due to the higher intensity of the re-entrant jet, this process continues for a larger time, until the clouds of vapor are pushed completely downstream, which will be discussed in the following stage.

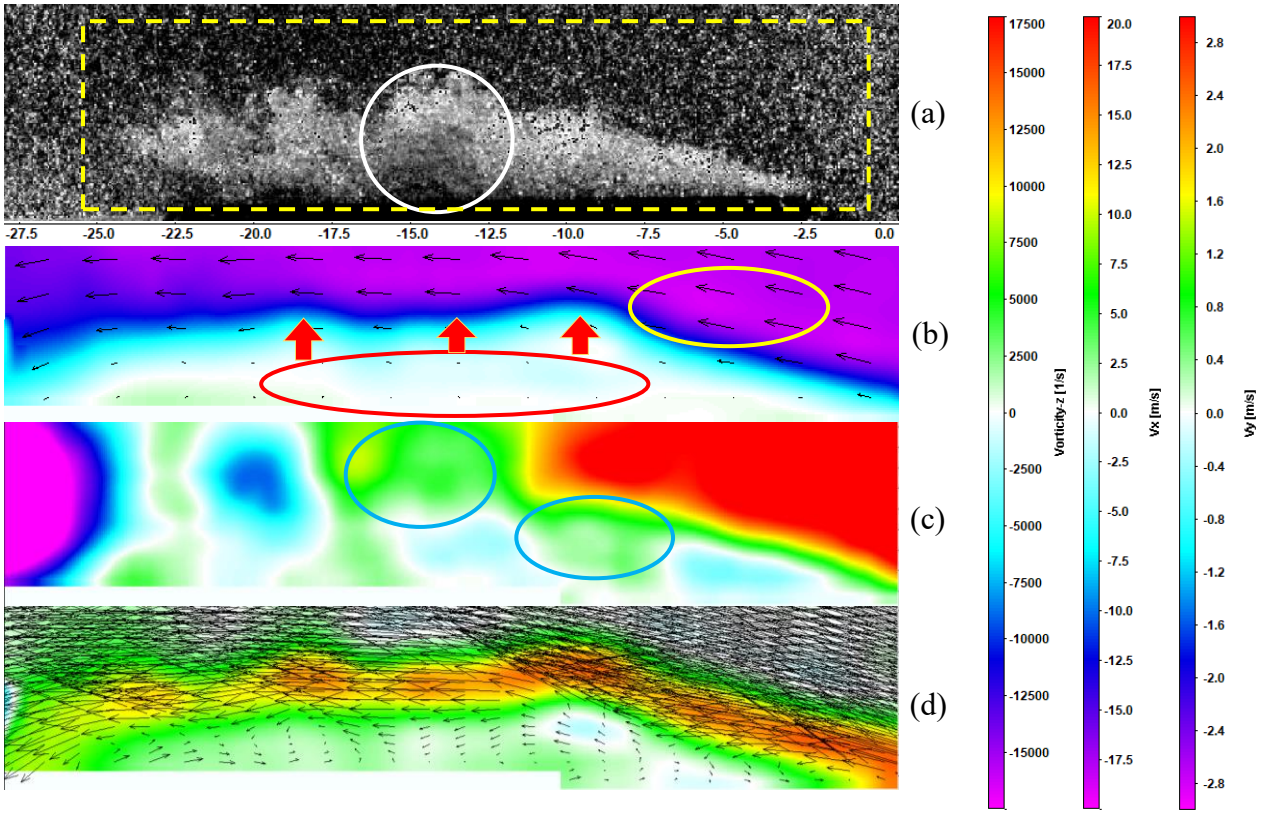

Figure 25. Cavity at time T_0 + 2 ms in the case of multi-clouds cavitation (test case #6). (a) Image of the cavity, (b, c) velocity field in the x and y directions, (d) vorticity fields. The velocity vectors are shown in pictures b and d to show the flow structure.

Like in the case of single cloud cavitation, the re-entrant jet thickens rapidly after the bulge is created and the main flow is slightly compressed (see figure 25b), creating a high-pressure zone on the upper right side of the bulge (yellow circle), and thus the break-off of the cavity as shown in figure 26 at T_0 + 2.4 ms and after. Figure 26a shows that the wavy sheet cavity is stretched rapidly, like in the growing process shown for single cloud cavitation in figures 23d and 23e. The difference, however, is that two clouds start to detach from the main cavity at almost the same time at T_0 + 2.8 ms (figure 26b), and the two clouds are both detached simultaneously at T_0 + 3.2 ms (figure 26c). They are eventually pushed downstream and start to collapse around T_0 + 3.6 ms (figure 26d).

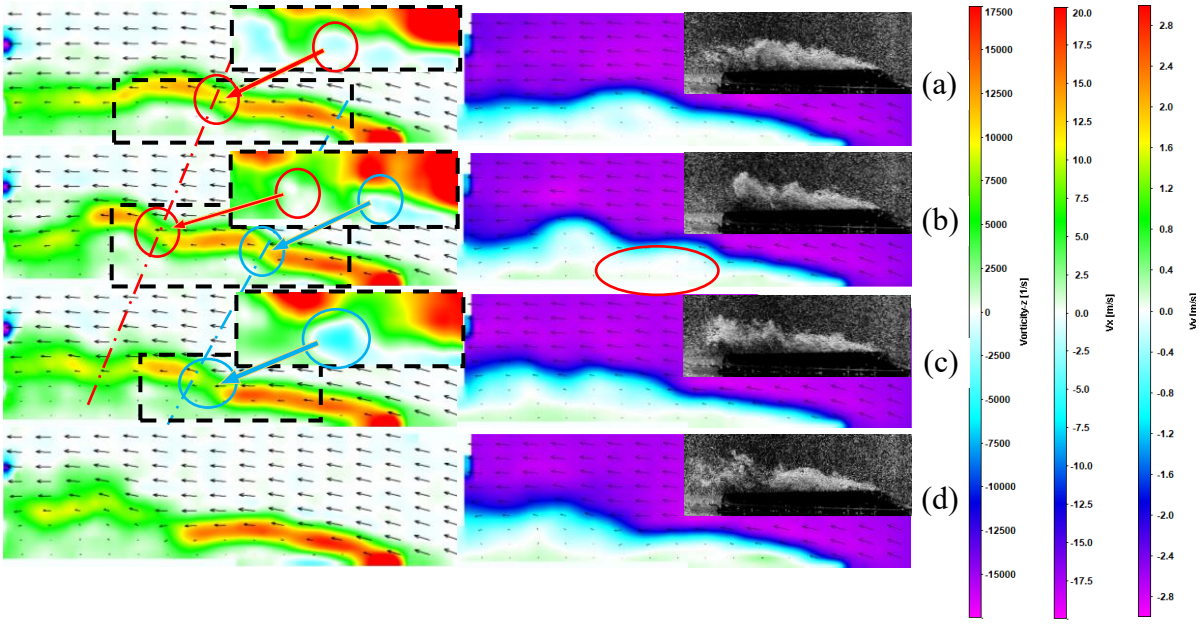

Figure 26. Break-off and convection of multi clouds cavitation (Test case #6)

Left: vorticity field and velocity vectors, V_y velocity component in the top image

Right: V_x velocity component and velocity vectors

Times T_0 + 2.4 ms (a), T_0 + 2.8 ms (b), T_0 + 3.2 ms (c) and T_0 + 3.6 ms (d)

These observations suggest that the slowdown of the re-entrant jet is the trigger for the cavity break-off: as the jet becomes unable to sustain a longer wavy sheet cavity, the main flow tends to intrude at the weakest point, i.e., at the middle of the re-entrant jet, thus cutting it as shown with the red circle on the vorticity field (figure 26a, left), and also the negative V_y in the same location. As can be seen from the V_x distribution (figure 26b, right), a small new re-entrant jet (red circle) is generated at the bottom wall.

During the break-off, as said previously, two clouds are formed. To explain it, let's take a closer look at the re-entrant jet evolution. In the previous section focused on single cloud cavitation, it has

been found that the re-entrant jet is not a pure reverse flow in the x direction, it is also composed of vortices in the z direction. Here at T_0 + 2.8 ms, three strong vortices are detected on both V_y and the vorticity field (figures 27b & 27c), which will generate the two cloud detachments. The first vortex was formed at the cavity leading edge during the growing phase (from T_0 to T_0 + 1.6 ms), by the interaction between the re-entrant jet and the main flow. At time T_0 + 2 ms (figure 25), the vortex has become strong enough to create a significant lift and form the bulge. In addition, it is pushed downstream by the main flow (see the local speed of about 7 m/s at T_0 + 2.4 ms). At the same time, a second vortex is created at the same initial position. At time T_0 + 2.8 ms, this second vortex is also pushed downstream, while a third vortex begins to form. The presence of the re-entrant jet creates favorable conditions for the convection of these 3 vortices, as it provides them with some additional energy en route. The strength of each vortex varies to some extent, depending on the magnitude of the re-entrant jet. When the vortex is not strong enough, as shown, for example at times T_0 + 1.2 ms and T_0 + 1.6 ms in figure 24, it will not generate a sufficient lifting effect to form a large bulge and lead to cloud shedding.

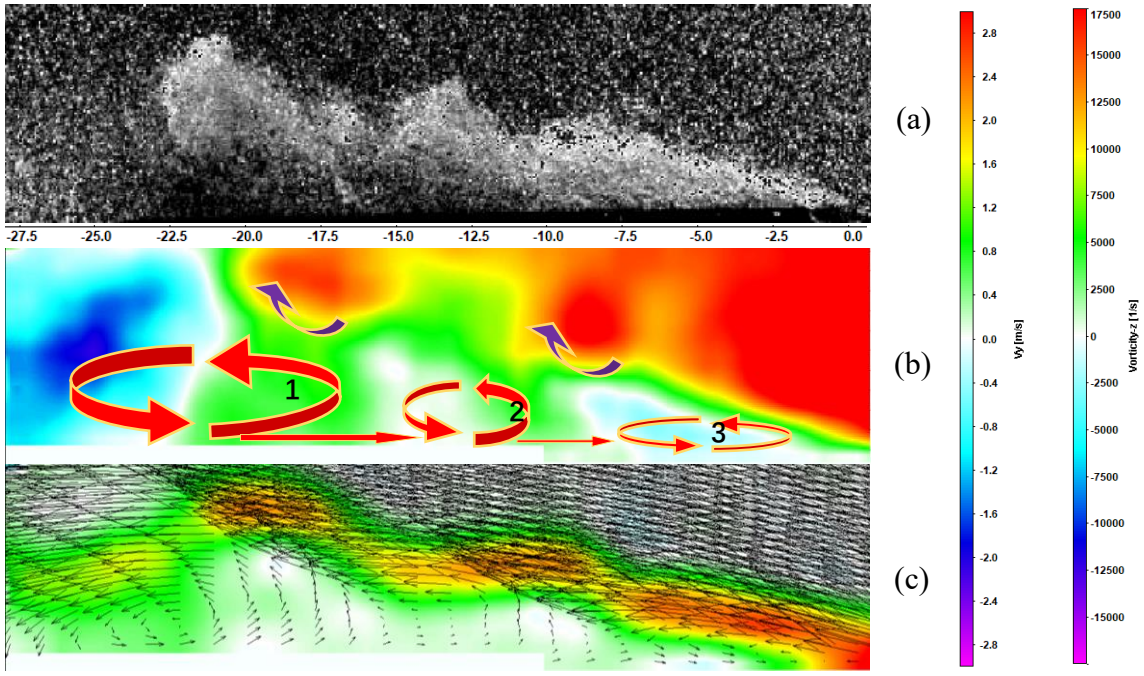

Figure 27. Structure of the re-entrant jet in a multi clouds configuration (test case #6) at T_0 + 2.8 ms, showing the mechanism of cloud formation. (a) shape of the sheet cavity, (b) V_y component, (c) vorticity field with velocity vectors.

As shown by the velocity field in the y direction, there is a strong lifting effect in the upper right of each vortex and a downward velocity component on the left side. This combination results in a stepped structure shown in the vorticity field, which enables the main flow to cut the cavity in between

two vortices. At T_0 + 2.8 ms, this process has started as indicated by the red and blue circles (see the left of figure 26b), and it is completed at T_0 + 3.2 ms, when the clouds are detached. At time T_0 + 3.6 ms, the clouds of vapor have moved downstream, and the re-entrant flow has turned into a stronger and thinner jet, as can be seen in the velocity field in the x direction (figure 26d), which is the starting point of a new cycle. Multi clouds cavitation is an extremely unstable situation that usually lasts for a few cycles. After that, the flow resumes to a single cloud periodical shedding configuration.

4.3 sheet cavitation

When the cavity is small, i.e. for test cases #1 to #3, no periodical instability is obtained, or the rear part of the cavity collapses before being detached, which makes the understanding of the flow evolution more challenging. Figure 28 shows a typical cavity evolution and V_x component of the velocity field from T_0 (start of the cavity growth) up to T_0 + 1.6 ms, for test case #3. Note that for these specific results, the interrogation window in the image post-processing has been decreased down to 16×16 pixels, to get more details in the area of the sheet cavity, which induces a significant increase of the uncertainty, up to 5 to 10%.

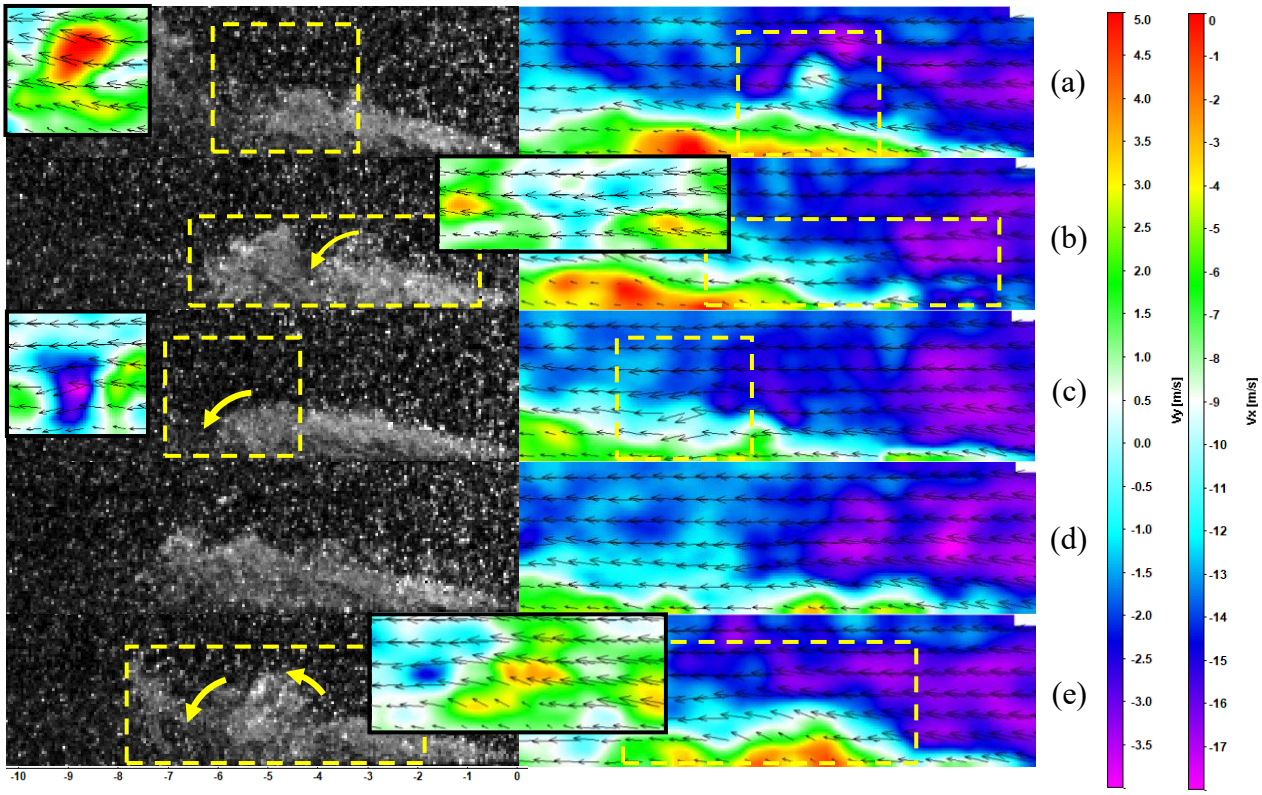

Figure 28. Sheet cavitation (test case #3): image of particles (left), V_x velocity component and velocity vectors (right) and V_y component (inserts).
(a) T_0, (b) T_0 +0.4 ms, (c) T_0 + 0.8 ms, (d) T_0 + 1.2 ms, (e) T_0 + 1.6 ms

It can be observed that the sheet cavity starts to grow at T_0 (figure 28a), forming a bulge-like structure at T0 + 0.4 ms (figure 28b). However, this bulge-like structure does not continue to develop into a detached, rotating cloud of vapor persisting during a significant time, like in the previous single- and multi-cloud cavitation cases. At T0 + 0.8 ms (figure 28c), this bulge-like structure is already detached from the main cavity and collapses before it can form a cloud (the collapse happens in less than 0.4 ms, so it is not captured at the 2500 fps frequency applied in PIV). Then it goes into the next "cycle" (figures 28d and 28e).

The velocity field in the x direction shows that during this process, there is no formation of re-entrant jet formation at all; however, there is a low (but still positive) velocity area close to the bottom wall. At T_0, a high-pressure is generated in this low-velocity area, resulting in a significant upward V_y component (see the yellow insert in figure 28a), which contributes to the formation of the bulge-like structure. At T_0 + 0.4 ms, a slightly downward V_y velocity component is generated between the bulge and the upstream part of the cavity (yellow insert in figure 28b), so the main flow begins to intrude into the low-speed region at the wall. At T_0 + 0.8 ms, this V_y flow velocity becomes stronger (yellow insert in figure 28c), which marks the full intrusion of the main flow, causing the low-speed area to shrink and eventually disappear. This mechanism prevents the production of vortices in the vicinity of the bottom wall. As a result, the cavity stays compressed against the bottom wall, and no detached cloud of vapor can be generated.

In this configuration, as the instability is milder and no re-entrant jet is generated, cavitation basically consists of an attached cavity at the venturi throat, and the downstream flow where some bubbles are just travelling and collapsing, with only minor effects on the baseline liquid flow. Note that a re-entrant jet is still generated intermittently, leading to minor shedding from time to time. However, these events do not induce any specific frequency, and are likely related to flow perturbations, such as fluctuations coming from the system of local roughness effects.

5. Conclusion

In this paper, the structure and instability of cavitating flows formed in the divergent part of a two-dimensional venturi have been analyzed using the velocity fields obtained from high-speed stereo PIV. It was shown that in spite of the small dimensions of the test section, the flow is quite two-dimensional, and the velocity fields obtained in different vertical planes from the center to the side of the channel were fairly identical.

Having access to the local flow velocity has enabled to propose a new objective definition for the length of the attached cavity, based on the length of the re-entrant jet or the value of the vorticity. The importance of measuring the pressure as close as possible to the cavitation area to define the cavitation number has been shown: in the present case, taking the average of the upstream and downstream pressures was found necessary to obtain all data points falling on the same curve for the evolutions of the cavity length or re-entrant jet length according to σ.

The comparison of the liquid and vapor time-averaged velocities at different positions has revealed two main areas of significant slip velocity between the two phases: (i) in the top half of the sheet cavity, where the largest vapor structures are not perfectly entrained by the liquid flow and have a lower speed, and (ii) the re-entrant jet area, where the intermittent nature of the jet, combined with the flow condensation at its tip, results in larger time-averaged velocities in the vapor, compared with the liquid.

By analyzing the flow time evolution, three different types of sheet/cloud cavitation were characterized, and some quantitative characterizations and qualitative analyses were carried out. Based on this study, an overview of these results is proposed here, focused on the primary mechanisms involved. As shown in figure 29, cloud cavitation is generally divided into four main stages: Growing, up-lift, cloud detachment, and cloud convection. At all steps, consistently with the recirculation cell model[13], the re-entrant jet plays a crucial role, since its structure and momentum trigger the flow evolution to the different behaviors.

As an extension to the re-entrant jet itself, the re-entrant region can be defined as the area between the mid-height of the cavity and the bottom wall, where the velocity is usually opposite to the main flow, or still in the same direction but much lower (typically less than 10% of the liquid flow above the sheet cavity). In this region, therefore, the strong interaction of the re-entrant jet with the main flow forms a strong vortex close to the cavity leading edge (just downstream of the venturi throat, as shown in figure 29a). The friction between the main flow and the re-entrant region induces a periodical detachment of this vortex and transfers downstream to form a series of vortices within the re-entrant region. This series of vortices lift the upper cavity above the bottom wall, thus maintaining an almost steady cavity region. This is the first stage of cloud cavitation: the growing stage.

If the reverse jet vanishes (case of the non-periodical instability in figure 29c), the vortex at the leading edge of the re-entrant region runs out of energy and disappears. This area is then compressed by the intrusion of the main flow and collapses. On the contrary, if the re-entrant jet remains strong

for a sufficient time, the detached vortex will grow dramatically as it moves downstream, forming a bulge (figure 29b), which initiates the up-lift stage. During this stage, the overall velocity of the re-entrant region decreases due to the growth of the vortex and bulge, becoming almost zero in the middle of the cavity (below the bulge).

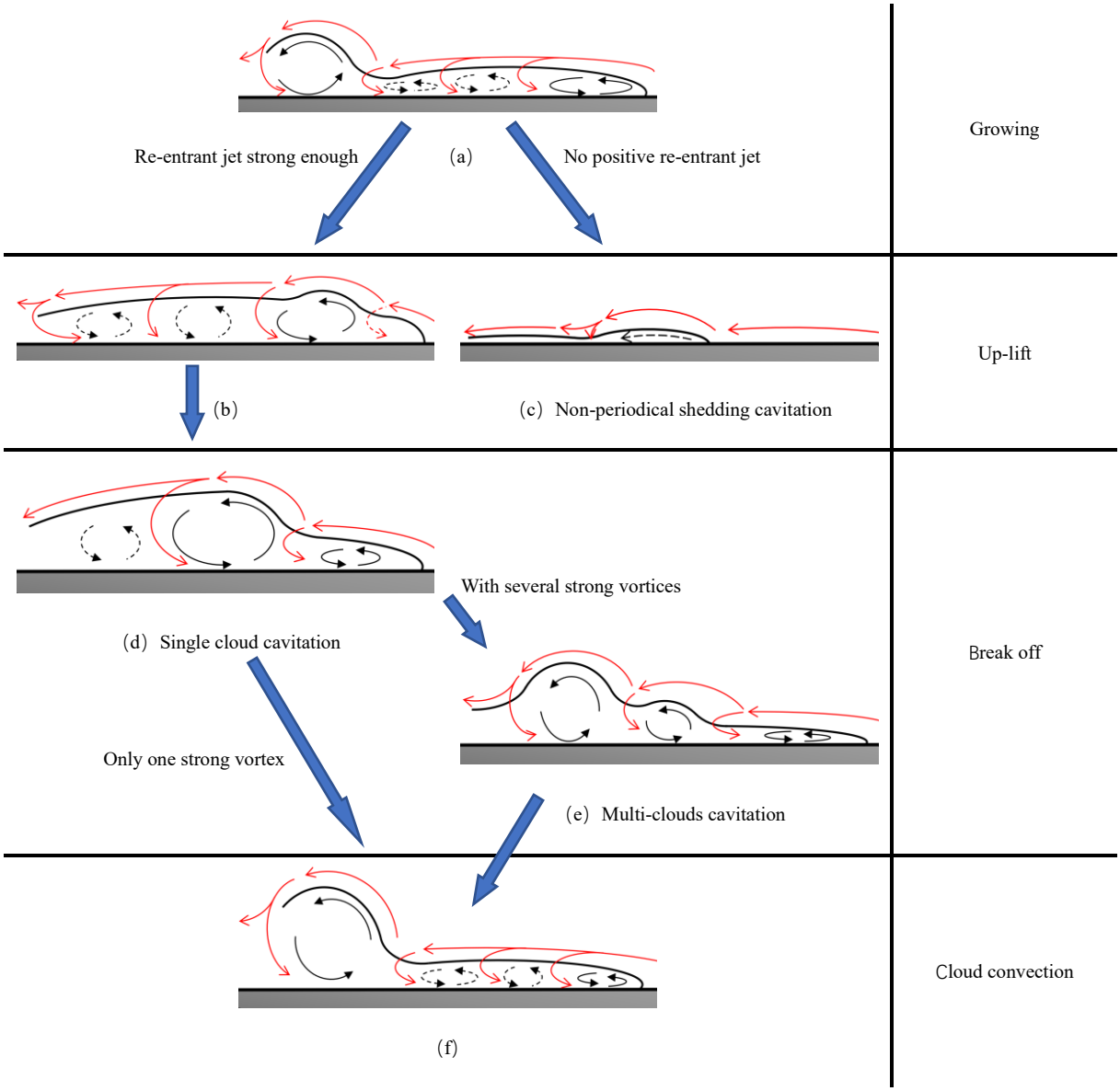

Figure 29. Schematic representation of the different steps in the three different types of behaviors shown in section 4

(a) growing stage, (b) bulge forming, (c) non-periodical shedding cavitation, (d) single cloud cavitation, (e) multi-clouds cavitation, (f) cloud convection

As the detached vortex or bulge grows up to a certain scale, it reduces the cross-section of the main liquid flow over the cavity, thus increasing the local pressure and causing this liquid flow to

deviate towards the gap between this vortex and the vortex at the leading edge of the re-entrant region, which results in the formation of a step-shaped re-entrant region. The single-cloud cavitation situation occurs when this mechanism perturbs the re-entrant jet at a point where no vortex at the leading edge of the re-entrant region is detached for a short period. However, when the re-entrant jet is strong enough, the action of the main flow is not sufficient to block the detachment of the next vortex, which will form a second high-intensity vortex. Then, because of the simultaneous lifting effects induced by these two vortices, a stair-stepping structure of the re-entrant region is obtained, as shown in figure 29e. This is the double cloud detachment typical of multi-cloud cavitation. In some cases, three clouds can even occur simultaneously, but this is a rare situation.

After that, in both cases of single-cloud and multi-cloud cavitation, the step-like structure is pushed downstream, and a new re-entrant region is created upstream. This “cloud convection” step is the final stage of the cycle (figure 29f).

Author’s Contribution

Kunpeng Long: Experiments, Data analysis, Writing of the original draft
Mingming Ge: Provided assistance for the experiments, Data validation
Annie-Claude Bayeul-Lainé: co-supervision of the work
Olivier Coutier-Delgosha: Supervision of the work, Writing, review & editing.

Acknowledgements

This research was performed at Arts et Métiers Paris Tech in the LFML research center (Laboratoire de Mécanique des Fluides de Lille), and in the Aerospace and Ocean Engineering Department at Virginia Tech. The authors wish also to express their gratitude to CSC (China Scholarship Center) for the continuous support.

Data Availability

Data available on request from the authors. The data that support the findings of this study are available from Kunpeng Long (kunpeng.long@ensam.eu), upon reasonable request.

References

[1] Dular M, Khlifa I, Fuzier S, et al. Scale effect on unsteady cloud cavitation[J]. Experiments in fluids, 2012, 53(5): 1233-1250.

[2] Furness R A, Hutton S P. Experimental and theoretical studies of two-dimensional fixed-type cavities[J]. 1975.

[3] Stutz B, Reboud J L. Experiments on unsteady cavitation[J]. Experiments in fluids, 1997, 22(3): 191-198.

[4] Arndt R E A, Song C C S, Kjeldsen M, et al. Instability of partial cavitation: a numerical/experimental approach[J]. 2000.

[5] Laberteaux K R, Ceccio S L. Partial cavity flows. Part 1. Cavities forming on models without spanwise variation[J]. Journal of Fluid Mechanics, 2001, 431: 1-41.

[6] Laberteaux K R, Ceccio S L. Partial cavity flows. Part 2. Cavities forming on test objects with spanwise variation[J]. Journal of Fluid Mechanics, 2001, 431: 43-63.

[7] Dular M, Bachert B, Stoffel B, et al. Relationship between cavitation structures and cavitation damage[J]. Wear, 2004, 257(11): 1176-1184.

[8] Coutier-Delgosha O, Stutz B, Vabre A, et al. Analysis of cavitating flow structure by experimental and numerical investigations[J]. Journal of Fluid Mechanics, 2007, 578: 171-222.

[9] Pham T M, Larrarte F, Fruman D H. Investigation of unsteady sheet cavitation and cloud cavitation mechanisms[J]. 1999.

[10] Park J T, Cutbirth J M, Brewer W H. Hydrodynamic performance of the large cavitation channel (LCC)[C]//Fluids Engineering Division Summer Meeting. 2003, 36975: 87-100.

[11] Knapp R T, Daily J W, HAMMITT F. G. 1970 Cavitation[J]. McGraw-Hill Book Company, London.

[12] Stanley C, Barber T, Rosengarten G. Re-entrant jet mechanism for periodic cavitation shedding in a cylindrical orifice[J]. International Journal of Heat and Fluid Flow, 2014, 50: 169-176.

[13] Zhang H, Zuo Z, Mørch K A, et al. Thermodynamic effects on Venturi cavitation

characteristics[J]. Physics of Fluids, 2019, 31(9): 097107.

[14] Callenaere M, Franc J P, Michel J M, et al. The cavitation instability induced by the development of a re-entrant jet[J]. Journal of Fluid Mechanics, 2001, 444: 223-256.

[15] Stutz B, Reboud J L. Experiments on unsteady cavitation[J]. Experiments in fluids, 1997, 22(3): 191-198.

[16] Leroux J B, Coutier-Delgosha O, Astolfi J A. A joint experimental and numerical study of mechanisms associated to instability of partial cavitation on two-dimensional hydrofoil[J]. Physics of fluids, 2005, 17(5): 052101.

[17] Gopalan S, Katz J. Flow structure and modeling issues in the closure region of attached cavitation[J]. Physics of fluids, 2000, 12(4): 895-911.

[18] Foeth E J, Van Doorne C W H, Van Terwisga T, et al. Time resolved PIV and flow visualization of 3D sheet cavitation[J]. Experiments in Fluids, 2006, 40(4): 503-513.

[19] Kravtsova A Y, Markovich D M, Pervunin K S, et al. High-speed visualization and PIV measurements of cavitating flows around a semi-circular leading-edge flat plate and NACA0015 hydrofoil[J]. International Journal of Multiphase Flow, 2014, 60: 119-134.

[20] Dular M, Bachert R, Stoffel B, et al. Experimental evaluation of numerical simulation of cavitating flow around hydrofoil[J]. European Journal of Mechanics-B/Fluids, 2005, 24(4): 522-538.

[21] Dular M, Bachert R, Schaad C, et al. Investigation of a re-entrant jet reflection at an inclined cavity closure line[J]. European Journal of Mechanics-B/Fluids, 2007, 26(5): 688-705.

[22] Khlifa I, Vabre A, Hočevar M, et al. Fast X-ray imaging of cavitating flows[J]. Experiments in fluids, 2017, 58(11): 1-22.

[23] Zhang G, Khlifa I, Coutier-Delgosha O. A comparative study of quasi-stable sheet cavities at different stages based on fast synchrotron x-ray imaging[J]. Physics of Fluids, 2020, 32(12): 123316.

[24] Ganesh H, Mäkiharju S A, Ceccio S L. Bubbly shock propagation as a mechanism for sheet-to-cloud transition of partial cavities[J]. Journal of Fluid Mechanics, 2016, 802: 37-78.

[25] Lush P A, Peters P I. Visualisation of the cavitating flow in a venturi type duct using high-speed cine photography[C]//Proceedings of the IAHR conference on operating problems of pump stations an power plants. 1982: 1-13.

[26] Pipp P, Hočevar M, Dular M. Numerical insight into the kelvin-helmholtz instability appearance in cavitating flow[J]. Applied Sciences, 2021, 11(6): 2644.

[27] Zhang G, Zhang D, Ge M, et al. Experimental investigation of three distinct mechanisms for the transition from sheet to cloud cavitation[J]. International Journal of Heat and Mass Transfer, 2022, 197: 123372.

[28] Leroux J B, Coutier-Delgosha O, Astolfi J A. A joint experimental and numerical study of mechanisms associated to instability of partial cavitation on two-dimensional hydrofoil[J]. Physics of fluids, 2005, 17(5): 052101.

[29] Fuzier S, Coudert S, COUTIER D. O. Two phase velocity measurements using LIF-PIV inside the cavitation sheet generated in a venturi[C]//of: 8 th International Conference on Multiphase Flow ICMF. 2013: 26-31.

[30] Ge M, Zhang G, Apte D, et al. Analysis of the slip velocity between the two phases in a high-speed cavitating flow[C]//APS Division of Fluid Dynamics Meeting Abstracts. 2021: M29. 003.